AGU PUBLICATIONS

JGR

Journal of Geophysical Research: Atmospheres

RESEARCH ARTICLE
10.1002/2016JD025852

Monthly top-down NO_x emissions for China (2005–2012): A hybrid inversion method and trend analysis

Zhen Qu[1], Daven K. Henze[1], Shannon L. Capps[1,2], Yi Wang[3], Xiaoguang Xu[3], Jun Wang[3], and Martin Keller[4]

[1]Department of Mechanical Engineering, University of Colorado Boulder, Boulder, Colorado, USA, [2]Now at Department of Civil, Architectural, and Environmental Engineering, Drexel University, Philadelphia, Pennsylvania, USA, [3]Center for Global and Regional Environmental Research, Department of Chemical and Biochemical Engineering, University of Iowa, Iowa City, Iowa, USA, [4]Department of Physics, University of Toronto, Toronto, Ontario, Canada

Key Points:
- We develop a new method for long-term high-resolution NO_2 inversion which efficiently captures trends and spatial variations of emissions
- NO_2 columns (9%) and NO_x emissions (16%) in China both increase in this period, while regional trends are found at province and city level
- NO_2 column trends can be significantly different from those of NO_x emissions, and meteorology can account for up to 30 of this difference

Supporting Information:
- Supporting Information S1

Correspondence to:
Z. Qu,
zhen.qu@colorado.edu

Citation:
Qu, Z., D. K. Henze, S. L. Capps, Y. Wang, X. Xu, J. Wang, and M. Keller, (2017), Monthly top-down NO_x emissions for China (2005–2012): A hybrid inversion method and trend analysis, *J. Geophys. Res. Atmos.*, *122*, 4600–4625, doi:10.1002/2016JD025852.

Received 31 AUG 2016
Accepted 15 MAR 2017
Accepted article online 22 MAR 2017
Published online 18 APR 2017

Abstract We develop an approach combining mass balance and four-dimensional variational (4D-Var) methods to facilitate inversion of decadal-scale total nitrogen oxides ($NO_x = NO + NO_2$) emissions. In 7 year pseudo-observation tests, hybrid posterior emissions have smaller normalized mean square error (NMSE) than that of mass balance when compared to true emissions in most cases and perform slightly better in detecting NO_x emission magnitudes and trends. Using this hybrid method, OMI NO_2 satellite observations and the GEOS-Chem chemical transport model, we find more than 30% increases of emissions over most of East China at the 0.5° × 0.667° grid cell level, leading to a 16% growth of emissions over all of China from 2005 to 2012, whereas emissions in several urban centers have decreased by 10–26% in the same period. From 2010 to 2012, a decline is found in the North China Plain, Hubei Province, and Pearl River Delta area, coinciding with China's enforcement of its twelfth "Five Year Plan." Changes in individual grid cell may be different from changes over the entire city or province, as exemplified by opposite trends in Beijing versus the Mentougou district of Beijing from 2005 to 2012. Also, NO_2 columns do not necessarily have the same trend as NO_x emissions due to their nonlinear response to emissions and the influence of meteorology, the latter alone which can cause up to 30% interannual changes in NO_2 columns. Compared to recent bottom-up inventories, hybrid posterior emissions have the same seasonality, smaller emissions, and emission growth rate at the national scale.

1. Introduction

Nitrogen oxides play a key role in atmospheric chemistry. They contribute to the formation of tropospheric ozone through reaction with volatile organic compounds (VOCs), and they lead to the formation of secondary organic and inorganic aerosols [*Crutzen*, 1979; *Haagen-Smit*, 1952; *McKeen et al.*, 1991; *Ryerson et al.*, 2001; *Chan et al.*, 2010]. These forms of air pollution lead to decreased visibility [*Haagen-Smit*, 1952], cardiac and respiratory morbidity [*Bhatnagar*, 2006; *Ghio et al.*, 2000; *Nel*, 2005], and acidification and eutrophication of waters when deposited in excess [*Driscoll et al.*, 2001; *Likens et al.*, 1972]. Though NO_x emissions in North America [*Kim et al.*, 2006; *Lamsal et al.*, 2011; *Russell et al.*, 2012; *Lu et al.*, 2015] and Western Europe [*Castellanos and Boersma*, 2012] have decreased in the past two decades, their emissions in China have increased rapidly due to economic development and urbanization since the turn of the century [*Stavrakou et al.*, 2008; *Lamsal et al.*, 2011; *Lin and McElroy*, 2011; *Zhao et al.*, 2013; *Mijling et al.*, 2013; *Jin and Holloway*, 2015; *Krotkov et al.*, 2016; *Cui et al.*, 2016; *Duncan et al.*, 2016; *Xia et al.*, 2016].

A comprehensive and accurate NO_x emissions inventory is an essential input for air quality modeling studies performed to support air quality regulations and further evaluate our understanding of atmospheric chemistry. One of the first comprehensive Asian emission inventories was developed by *Streets et al.* [2003] for the year 2000 to support the Transport and Chemical Evolution over the Pacific (TRACE-P) campaign. This inventory was then updated by *Zhang et al.* [2009] for the year 2006 for National Aeronautics and Space Administration (NASA)'s Intercontinental Chemical Transport Experiment-Phase B (INTEX-B) mission. Recently, *Li et al.* [2015] developed a new anthropogenic emission inventory for Asia (MIX) for the year 2008 and 2010 to support the Model Inter-Comparison Study for Asia (MICS-Asia) and Task Force on Hemispheric Transport of Air Pollution (TF HTAP). A long-term Regional Emission Inventory in Asia (REAS) was also developed by

Ohara et al. [2007] for the years 1980–2003 and was updated for 2000–2008 as version 2.1 by *Kurokawa et al.* [2013]. These bottom-up NO_x emission inventories have provided essential information for atmospheric chemistry and climate studies but are subject to substantial uncertainties due to limited knowledge of emission factors and fuel combustion and often take years to compile [*Streets et al.*, 2003; *Ohara et al.*, 2007; *Zhang et al.*, 2007, 2009; *Kurokawa et al.*, 2013; *Li et al.*, 2015]. It is particularly difficult to precisely quantify NO_x emissions with this approach in China, since emissions originate from a complex mixture of sources with different technologies and levels of combustion efficiencies and a large spatial variation [*Streets et al.*, 2003].

Alternatively, satellite observations can improve our understanding of NO_x sources and chemistry by constraining emission inventories through inverse modeling techniques. Several statistical approaches to developing such constraints have been considered in previous studies. *Beirle et al.* [2011] used an exponentially modified Gaussian (EMG) method to determine both NO_x emissions and lifetime in a megacity (Riyadh) from NO_2 column observations from the Ozone Monitoring Instrument (OMI). *Duncan et al.* [2013] estimate changes of NO_x emissions in a grid box containing power plants by scaling changes of NO_2 columns with the product of changes in emissions in power plants and a parameter determined by the chemical lifetime of NO_x, meteorology, and factors affecting partitioning of NO_x. These two approaches were evaluated in *de Foy et al.* [2014], with results showing that the EMG approach requires NO_2 plumes to be consistently in the same direction [*Valin et al.*, 2014], and multiple years averages are required for an accurate result, whereas the box model method can more robustly and precisely estimate NO_x emissions at seasonal scales.

Other approaches have combined satellite retrievals with simulations from chemical transport models. An extended Kalman filter algorithm is used to estimate NO_x emissions in East China [*Mijling and van der A*, 2012] and NO_x emissions in the city of Nanjing during the 2014 Youth Olympic Games [*Ding et al.*, 2015]. *Miyazaki et al.* [2012] used an ensemble Kalman filter approach to optimize global daily NO_x emissions from an assimilation of OMI NO_2 columns. Monte Carlo sampling of a linear statistical relationship between tropospheric NO_2 column and NO_x emissions is applied [*Konovalov et al.*, 2006] to improve NO_x emissions in Western Europe, based on measurements from GOME and Scanning Imaging Absorption Spectrometer for Atmospheric Chartography (SCIAMACHY). Two approaches closely related to our study are mass balance and 4D-Var. The mass balance approach has been used to optimize global NO_x emissions based on the ratio of observed and simulated NO_2 column [*Martin et al.*, 2003a; *Toenges Schuller et al.*, 2006; *Boersma et al.*, 2008; *Lamsal et al.*, 2011; *Ghude et al.*, 2013; *Vinken et al.*, 2014a, 2014b; *Castellanos et al.*, 2014; *Gu et al.*, 2016]. This approach, originally formulated for global models with resolutions exceeding hundreds of kilometers, has not rigorously taken into account the impact of emissions in one model grid cell on concentrations in neighboring cells, which may not be suitable for resolutions approaching a few kilometers [*Turner et al.*, 2012]. The perturbation mass balance approach, as used in *Lamsal et al.* [2011], *Vinken et al.* [2014a, 2014b], and *Castellanos et al.* [2014] is a first-order approximation of the influence of nonlinear chemistry. More explicit treatment of chemistry and transport can be accomplished using the 4D-Var approach [*Müller and Stavrakou*, 2005; *Stavrakou et al.*, 2013; *Xu et al.*, 2013], in which information about model error is propagated backward in time through the modeled chemistry and transport, and all NO_x-related chemical processes included in the forward model are used to improve NO_x emissions. While rigorous, such approaches are more computationally demanding, requiring an adjoint model and an interactive optimization procedure.

Many of these top-down approaches have been previously used to constrain NO_x emissions in China. These include studies of the seasonality of NO_x emissions. For instance, an emission peak in winter was found by *Wang et al.* [2007] in a 3 year average of 1997, 1998, and 2000, and *Gu et al.* [2014] found higher anthropogenic NO_x emissions in winter and summer than spring (and possibly fall, although this comparison is hindered by uncertainties in the bottom-up inventory). Satellite inversions were also used for estimations of national NO_x budget, for which 6.8 Tg N yr^{-1} was estimated based on OMI observations in July 2008 [*Lin et al.*, 2010], and an optimization of 6.9 Tg N yr^{-1} was obtained using a daily inversion of OMI and GOME-2 for 2011 [*Gu et al.*, 2014]. A 20% reduction of NO_x emissions from January 2008 compared to January 2009 was estimated by *Lin and McElroy* [2011], indicative of an economic downturn in China; however, this decrease was not evident in annual average NO_2 column densities[*Krotkov et al.*, 2016].

Our objective here is to develop an effective inversion approach for a monthly-scale, 8 year top-down NO_x emission inventory over China, which does not include Taiwan in this study. Before doing this, we improve the performance of 4D-Var and mass balance approaches, compare how they optimize emissions, and evaluate the causes of differences between these approaches (section 3.1–3.3). We then seek a way to combine

these two methods to provide a favorable blend of accuracy and efficiency (section 3.4). Trends of posterior NO_x emissions using this hybrid inversion method are analyzed in section 4. In section 5, these trends are evaluated through comparison to other top-down studies, bottom-up inventories, and in situ measurements. Uncertainties in this top-down emission inventory are discussed in section 6.

2. Model and Observations

2.1. NO_x Simulation Using GEOS-Chem and Its Adjoint Model

To estimate NO_2 column density over China from January 2005 to April 2013, we use the GEOS-Chem adjoint model (http://wiki.seas.harvard.edu/geos-chem/index.php/GEOS-Chem_Adjoint) v35f based on version 8-02-01 of the GEOS-Chem 3-D chemical transport model (http://www.geos-chem.org) with relevant updates and bug fixes up through version 9. Our simulations are driven by assimilated meteorology data from the Goddard Earth Observing System (GEOS-5) of the NASA Global Modeling and Assimilation Office (GMAO) [*Bey et al.*, 2001]. These meteorological data are available for years 2004 through mid-2013; hence, we study OMI data in this time range. It has a horizontal resolution of 0.5° × 0.667° and 72 vertical layers. We employed the nested-grid version of GEOS-Chem in this study at a native horizontal resolution of 0.5° × 0.667° over East Asia (70°E–150°E, 0°N–50°N) and 47 layers from the surface to ~0.01 hPa. Boundary conditions are generated from a global simulation with 4° × 5° horizontal resolution. The tropospheric oxidant chemistry in GEOS-Chem includes a detailed ozone-NO_x-hydrocarbon chemical mechanism [*Bey et al.*, 2001]. Partitioning of NO_x and nitric acid between the gas and particle phases is calculated using aerosol scheme from *Park et al.* [2004]. Uptake of NO_2 and NO_3 on aerosol surfaces is described in *Martin et al.* [2003b]. Uptake of N_2O_5 by aerosols is from *Evans and Jacob* [2005]. Wet and dry deposition of gases and aerosols are described in *Liu et al.* [2001].

We use anthropogenic emissions (NO_x, SO_2, NH_3, CO, NMVOCs, and primary aerosols) in 2010 to drive simulations from 2005 to 2013. These emissions are taken from HTAP inventory version 2 [*Janssens-Maenhout et al.*, 2015], which is a bottom-up emission inventory consisting of monthly 0.1° × 0.1° grid maps and is compiled using different regional gridded inventories, including the Model Inter Comparison Study in Asia (MICS-Asia)'s for Asian countries. The MICS-Asia inventory consists of REAS inventory 2.1 for the whole area of Asia [*Kurokawa et al.*, 2013], Multiresolution Emission Inventory for China (MEIC; http://www.meicmodel.org), a high-resolution NH_3 emission inventory (PKU-NH_3) [*Huang et al.*, 2012], Indian emission inventory (ANL-India) [*Lu et al.*, 2011], and the official Korean emission inventory [*Lee et al.*, 2011]. Emissions from the HTAP inventory are monthly average values. Diurnal and day-of-week variability are applied internally in GEOS-Chem.

Nonanthropogenic emissions are from each simulated year, with 3-hourly biomass burning emissions from GFED4 [*Giglio et al.*, 2013] generated by HEMCO stand-alone model [*Keller et al.*, 2014]. NO_x emissions from lightning are specified using the cloud top height parameterization from *Price and Rind* [1992], vertical distribution profile from *Pickering et al.* [1998], local redistribution method from *Sauvage et al.* [2007], and further satellite constraints from *Murray et al.* [2012]. Soil NO_x emissions are calculated by Yienger and Levy's algorithm [*Yienger and Levy*, 1995] with soil canopy reduction factors [*Wang et al.*, 1998]. Monthly NO_x emissions in China from different sectors and changes of nonanthropogenic emissions from year to year are shown in Figure 1. In the pseudo-observation test, we use anthropogenic emissions in 2006 from the INTEX-B mission [*Zhang et al.*, 2009] for all studied years and biomass burning inventory from GFED3 [*van der Werf et al.*, 2010] for 2005 to 2011 and GFED4 for 2012.

The GEOS-Chem adjoint model was developed specifically for inverse modeling of aerosol and gas emissions using the 4D-Var method by *Henze et al.* [2007]. It includes the adjoint for model processes of aerosol thermodynamics, chemistry, convection, turbulent mixing, advection, and wet removal. This model provides an efficient way to calculate sensitivity of model variables (e.g., column densities and concentrations) to model parameters (e.g., emissions) [*Henze et al.*, 2009; *Kopacz et al.*, 2009].

2.2. Tropospheric NO_2 Columns From OMI

The OMI aboard the Earth Observing System (EOS) Aura satellite observes visible and ultraviolet (264–504 nm) solar backscatter radiation, which can be used to retrieve tropospheric NO_2 column densities with the Differential Optical Absorption Spectroscopy (DOAS) method. The instrument has a Sun-synchronous polar orbit with a 13:40 equatorial overpass time. Since August 2004, OMI has collected daily global coverage measurements in a spatial resolution of 13 km along track and 24 km across track in the nadir view, and operational data products are provided since October 2004.

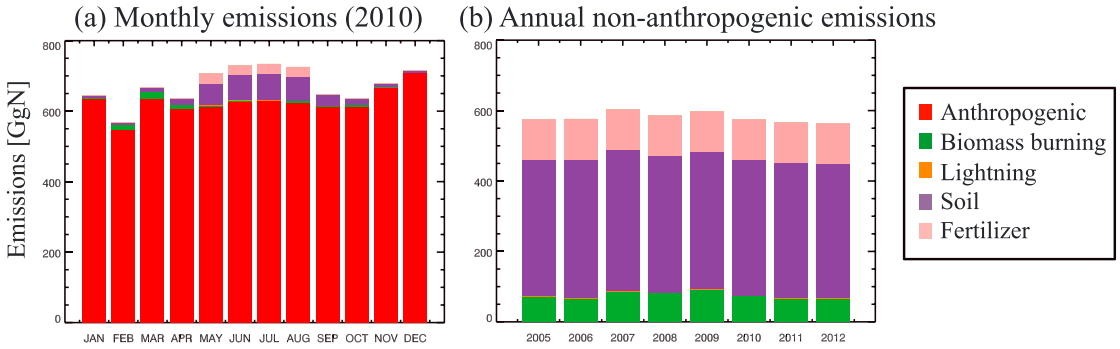

Figure 1. Distribution of monthly and annual NO_x emissions from each sector in China. (a) Monthly NO_x emissions in 2010. (b) Annual nonanthropogenic NO_x emissions from 2005 to 2012.

For this study, we use the NASA standard product OMNO2 (Level 2, Version 2.1) tropospheric NO_2 slant column density from NASA Goddard Earth Sciences Data and Information Services Center (GES DISC) (http://disc.sci.gsfc.nasa.gov/Aura/data-holdings/OMI/omno2_v003.shtml). In the retrieval algorithm, total slant column density (SCD) is obtained from OMI spectra by DOAS; stratospheric SCDs are subtracted from the destriped total SCD using a Stratosphere Troposphere Separation (STS) algorithm; tropospheric SCDs are then converted to vertical column density (VCD) using tropospheric air mass factors (AMFs), which are a function of the shape of the NO_2 vertical profile, temperature profile, scattering weights, terrain albedo, tropopause pressure, cloud fraction, cloud top pressure, viewing zenith angle, and solar zenith angle [*Bucsela et al.*, 2006, 2013; *Celarier et al.*, 2008; *Platt and Stutz*, 2008]. Errors in tropospheric NO_2 retrievals come from each of these three steps and are associated with the total SCD, separation of the stratosphere and troposphere, and calculation of the tropospheric AMF. These uncertainties play an important role in our maximum likelihood estimation and will be discussed further in section 3.1.1.

In all of our simulations, we calculate the air mass factor (AMF) for GEOS-Chem simulated NO_2 columns (AMF_{GC}) following equations (1) to (4) in *Bucsela et al.* [2013]. Here AMF_{GC} is expressed as the ratio of the sum of slant subcolumns in the troposphere (S) to the sum of vertical subcolumns in the troposphere (V):

$$\mathrm{AMF}_{\mathrm{GC}}(i,j) = \frac{S}{V} \tag{1}$$

where

$$S = \kappa \Sigma_{l \text{ in the troposphere}} \mathrm{MR}(i,j,l)(P(i,j,l) - P(i,j,l+1))\mathrm{SCW}_{\mathrm{OMI}}(i,j,l) \tag{2}$$

$$V = \kappa \Sigma_{l \text{ in the troposphere}} \mathrm{MR}(i,j,l)(P(i,j,l) - P(i,j,l+1)). \tag{3}$$

Here MR is the mixing ratio of NO_2, κ is a unit conversion constant, P is the pressure at the center of the GEOS-Chem grid, SCW_{OMI} is the scattering weight linearly interpolated from OMI product to GEOS-Chem grid using the scattering weight pressure from the Level 2 product and pressure at the center of each model grid cell, with application of temperature correction following equation (4) of *Bucsela et al.* [2013]. This AMF is then used for conversion of GEOS-Chem NO_2 vertical column densities to SCDs, which are directly comparable to tropospheric SCDs calculated using OMI retrieval products,

$$\mathrm{SCD}_{\mathrm{GC}}(i,j) = \mathrm{AMF}_{\mathrm{GC}}(i,j)\Sigma_{l \text{ in the troposphere}} c(i,j,l)h(i,j,l) \tag{4}$$

where c is simulated NO_2 concentration (molecules cm^{-3}) and h is the height of the box. We screen OMI observations using retrieval quality flags and exclude data with row anomalies (http://projects.knmi.nl/omi/research/product/rowanomaly-background.php). Only positive tropospheric column densities in "cloud-free" (cloud fraction <20%) columns, with solar zenith angle <75°, and with viewing zenith angle <65° are used. The bias introduced by only using positive NO_2 column density is small for this study, as the monthly mean values of the NASA standard retrievals are negative in less than 5% of the grid cells covering China (mostly in western China). The absolute values of negative monthly means are all less than 1.7×10^{15} molecules cm^{-2}

during the studied period, with 78% of these absolute values less than 1×10^{15} molecules cm^{-2}. We also look at trends of NO_2 columns after eliminating data affected by row anomalies throughout the period.

In addition, we compare the trend of OMI NO_2 columns from the NASA standard product with that from the DOMINO (Level 2, Version 2.0) product (http://www.temis.nl/airpollution/no2.html). This destriped product is derived using the KNMI combined assimilation approach. We screen these observations using the tropospheric column flag and eliminate data when the surface albedo is larger than 0.3 as suggested by the DOMINO data user manual (http://www.temis.nl/docs/OMI_NO2_HE5_2.0_2011.pdf). Filtering criteria for positive tropospheric column density, cloud fraction, solar zenith angle, and viewing zenith angle follow those used with the NASA standard product. However, unless otherwise noted, OMI data referred to in our work are that from the NASA standard product OMNO2 described above.

3. Inversion Methods, Validations, and Comparisons

3.1. The 4D-Var Approach

We use an adjoint-based 4D-Var approach to constrain emissions. Considering anthropogenic emissions as model parameters, $E(i,j)$, in each grid cell (i,j), a linear parameter scaling factor is defined as $\sigma(i,j) = E(i,j)/E_a(i,j)$, where $E_a(i,j)$ are prior emissions values. A cost function, $J(\boldsymbol{\sigma})$, is used to measure the departure of the emission scaling factors from their prior estimates weighted by the prior error covariance matrix, plus the sum of squared error between the model and observations over time, weighted by the observational error covariance matrix. A $\boldsymbol{\sigma}$ that minimizes the cost function balances the objectives of improving model performance while ensuring the model not unreasonably deviate from its prior state. Here

$$J(\boldsymbol{\sigma}) = \frac{1}{2}\Sigma_{\mathbf{c}\in\Omega}\left(\mathcal{H}\mathbf{c} - \mathbf{SCD_{obs}}\right)^T \mathbf{S_{obs}^{-1}}(\mathcal{H}\mathbf{c} - \mathbf{SCD_{obs}}) + \frac{1}{2}\gamma_r\left(\boldsymbol{\sigma} - \boldsymbol{\sigma_a}\right)^T \mathbf{S_a^{-1}}\left(\boldsymbol{\sigma} - \boldsymbol{\sigma_a}\right) \quad (5)$$

where $\mathcal{H}$ maps the species concentration vector $\mathbf{c}$ to observation space, $\mathbf{c_{obs}}$ is the vector of species observations, $\boldsymbol{\sigma_a}$ is the prior estimate of the emission scaling factor, $\mathbf{S_a}$ and $\mathbf{S_{obs}}$ are error covariance matrices of the emission scaling factors and observations, respectively, γ_r is a regularization parameter, and Ω is the domain (in time and space) where observations are available. The first term is referred to as the "prediction error," and the second term is referred to as the "parameter error." In this study, $\mathcal{H}$ is the operator that converts GEOS-Chem simulated NO_2 concentration, $\mathbf{c}$, to NO_2 SCD, SCD_{GC} using equations (1) to (4), SCD_{OMI} is NO_2 SCD from the OMI Level 2 product, and $\boldsymbol{\sigma_a}$ is the prior emission scaling factor, which is a uniform vector of the ones when assimilating OMI NO_2 observations. Specification of other variable values is discussed in section 3.1.1.

3.1.1. Model Parameters and Optimization

Slant column densities from OMI at each observation time and site are used to constrain monthly anthropogenic NO_x emissions. The observation error covariance matrix, $\mathbf{S_{obs}}$, is assumed to be diagonal. Absolute uncertainties of these diagonal values are read from NASA OMNO2 L2 products for each individual OMI observation. On average, the tropospheric slant column uncertainty of OMI is estimated to be $\sim 0.7 \times 10^{15}$ molecules cm^{-2} [*Boersma et al.*, 2008; *Castellanos and Boersma*, 2012]. To reduce the influence of observations below the OMI detection limit, which mainly occur in remote locations, we conservatively assume an absolute uncertainty of 1.0×10^{15} molecules cm^{-2}, and we add this value to $\mathbf{S_{obs}}$.

Emissions from several species and sectors can have an influence on NO_2 column density. In order to identify a subset of these to adjust during the optimization, we consider the sensitivity of the cost function to grid-scale emission scaling factors for several species and sectors in four selected months, shown in Table 1. Sensitivities with respect to NO_x emissions are much higher than those of other species in all studied months. Sensitivities to anthropogenic NO_x emissions are about 2 orders of magnitude higher than other sectors in January, April, and October. In summertime (e.g., July), NO_x emissions from lightning have the largest sensitivities. In our 4D-Var inversions, we only allow emission scaling factors for anthropogenic NO_x to be adjusted, as these have the largest impact on $J(\boldsymbol{\sigma})$, in general, and are the most likely drivers of trends in total NO_x emissions, although we recognize that here they serve as a proxy for adjustments to total NO_x emissions in the inversion.

Uncertainties of the prior emission scaling factors are specified in the error covariance matrix, $\mathbf{S_a}$. Comparisons from *Li et al.* [2015] show that Asian NO_x emissions between MIX and the Emission Database for Global Atmospheric Research (EDGAR v4.2) inventory are different by about 20%, while sector level differences are even larger with a 48% discrepancy in residential emissions. Uncertainties in individual grid cells are expected to be larger than this average over the entire domain. For convenience, we use a constant average uncertainty

Table 1. Top Five Sensitivities of Adjoint Forcing to Emission Scaling Factors Over East Asia in 2010

	Sector	Sensitivity
Jan	NO_x ANTH[a]	−355 to 13,262
	NO_x BBN[b]	−2 to 601
	CO ANTH[a]	−43 to 148
	SO_2 ANTH[a]	−8 to 101
	CO BBN[b]	0–29
Apr	NO_x ANTH[a]	−105 to 1,294
	NO_x BBN[b]	−18 to 39
	NO_x LIGH[c]	−7 to 24
	NO_x SOIL	−7 to 13
	ISOP[d]ANTH[a]	−28 to 6
Jul	NO_x LIGH[c]	−6 to 4,011
	NO_x ANTH[a]	−12 to 113
	NO_x SOIL	−4 to 5
	CO ANTH[a]	0–4
	ISOP[d]ANTH[a]	−2 to 2
Oct	NO_x ANTH[a]	−234 to 2,570
	NO_x BBN[b]	−9 to 27
	NO_x LIGH[c]	−1 to 29
	NO_x SOIL	−6 to 8
	CO ANTH[a]	−2 to 6

[a]Anthropogenic emissions.
[b]Biomass burning emissions.
[c]Lightning emissions.
[d]Isoprene.

of 40% for all grid cells in the studied domain; the regularization parameter γ_r is then used to adjust the magnitude of the penalty term using an L curve [*Hansen*, 1999] and total error minimization [*Henze et al.*, 2009] for January 2010 (Figure S1 in the supporting information). Values of the regularization parameters in other months are scaled by the number of observations (counting only those filtered by criteria described in section 2.2) with respect to the value of γ_r in January. These values are shown in Table S1. Most previous NO_2 inversion studies using coarse resolution models have not accounted for spatial correlation in emissions across grid cells [e.g., *Martin et al.*, 2003a; *Müller and Stavrakou*, 2005; *Mijling and van der A*, 2012]. With the finer resolution used in our study, the emission correlation length scale may be longer than that of our model's horizontal resolution [*Turner et al.*, 2012], and errors are therefore correlated between adjacent grid cells. In this study, we assume an exponentially decaying error correlation with a constant decay distance of 150 km, whose inverse is calculated using the algorithm described in *Singh et al.* [2011]. Thus, an isolated high emission in one grid cell (not surrounded by other high-emissions sources) is allowed to decrease by at most 90% within a distance of three grid cells; however, we recognize that this treatment is only approximate and that the actual error correlation length scale in China is likely different and spatially variable. We minimize the cost function using the quasi-Newton L-BFGS-B gradient-based optimization technique [*Byrd et al.*, 1995; *Zhu et al.*, 1994], in which the gradient of the cost function $J(\boldsymbol{\sigma})$ with respect to the control parameter $\boldsymbol{\sigma}$ is calculated using the adjoint method. The adjoint model is driven by a forcing term, which is the error weighted difference between predicted and simulated NO_2 slant columns. Inversions are considered to have converged when the cost function decreases by less than 1% in three consecutive iterations.

3.1.2. Evaluation Using Pseudo-Observations

We evaluate our 4D-Var inversion by designing an inverse problem with a known solution. Anthropogenic emissions in 2006 from the INTEX-B mission [*Zhang et al.*, 2009] are used to generate 135,915 pseudo-observations for the whole month for January 2010, by sampling the model simulation at OMI overpass times. Hourly average tropospheric slant column densities from GEOS-Chem within 30 min of each OMI observation time and location are saved and used as pseudo-observations, which are assumed to have the same relative uncertainties as the real OMI observation at that corresponding time and location. Random noise is added to the observations according to the variance in $\mathbf{S_{obs}}$. Emissions used in this simulation are therefore true emissions for the pseudo-observations.

Our inverse modeling tests assimilate these pseudo-observations, starting from simulations whose anthropogenic NO_x emissions across the entire model domain are scaled to 0.5 or 1.5 times the product of true emissions and random noise. We refer to these two experiments as $\boldsymbol{\sigma_a} = 0.5$ and $\boldsymbol{\sigma_a} = 1.5$ in the following text. The random noise is normally distributed with mean of 1, standard deviation of 0.1, and spatial correlation described by $\mathbf{S_a}$. Only random noise within the range of 0.6 to 1.4 is applied to the true emissions. These scaled emissions therefore mimic the spatial correlation of NO_x emissions. The off-diagonal terms of $\mathbf{S_a}$ introduce more regularization for the inversion; consequently, the localized corrections with off-diagonal error covariance matrix are more smoothed out than those that result when using a diagonal error covariance matrix.

Comparisons of posterior emissions and prior emissions for these two cases are shown in Figure 2. In an ideal case (not considering errors in the observation or prior), emissions scaling factors would all converge to a mean of one after the inversion. However, in the $\boldsymbol{\sigma_a} = 0.5$ and $\boldsymbol{\sigma_a} = 1.5$ cases, scaling factors mainly change in Eastern China, where NO_2 column densities are higher and have larger forcing to drive the inversion. Therefore, emissions in several grid cells in this case still fall close to the $y = 0.5x$ and $y = 1.5x$ line after the inversion.

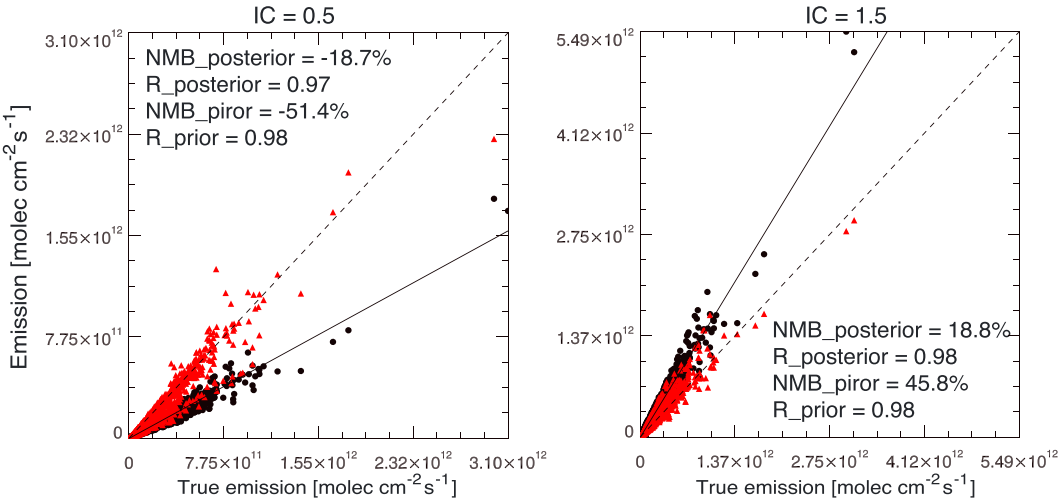

Figure 2. The 4D-Var emission scaling factors in pseudo-observation tests for σ_a = 0.5 and σ_a = 1.5. Inversions are performed with off-diagonal error covariance matrix. The black dots are prior emissions, while red triangles are posterior emissions.

The asymmetry of changes in emission scaling factors and emissions for σ_a = 0.5 and σ_a = 1.5 is caused by the dependence of initial conditions in the maximum likelihood estimation and the nonlinear response of NO_2 column changes to changes in NO_x emissions, which has been pointed out by *Stavrakou et al.* [2008]. This behavior is also seen in the pseudo-observation tests for the mass balance approach in section 3.2.2. NMSE and correlation coefficient of the posterior and initial emissions compared to true emissions are shown in Table 2. NMSE of posteriors have decreased by 88% (σ_a = 0.5) and 76% (σ_a = 1.5) after 4D-Var inversions. Correlation coefficients do not have big changes after the inversions.

3.2. Mass Balance Approach

The general idea of a mass balance inversion [*Martin et al.*, 2003a] is to estimate a top-down emission, $E_t(i,j)$, by scaling prior emissions, $E_a(i,j)$, by the ratio of the observed NO_2 slant column density, $SCD_{obs}(i,j)$, to the modeled NO_2 slant column density, $SCD_{GC}(i,j)$, for each grid cell (i,j). An averaging kernel may also be used to account for the impact of emissions from neighboring grid cells [*Toenges Schuller et al.*, 2006; *Boersma et al.*, 2008]. Detailed derivation of mass balance equations are shown in Appendix A. The weighting of errors in equation (A9) returns a maximum likelihood estimation; treatment of emission as lognormally distributed may yield a posterior emission that is smaller than both $E_a(i,j)$ and $E_t(i,j)$, because the posterior mode is smaller than its mean for a lognormal distribution. An example of this is shown in Figure 3.

3.2.1. Impact of Chemistry and Transport on Mass Balance Inversions

We first test the impact of horizontal transport of tracers across model grid columns and the nonlinear chemical relationship between NO_x emissions and NO_2 columns on the performance of mass balance inversions performed for a half month (first to sixteenth) simulation in January 2010, with real observations from OMI and anthropogenic emissions from the HTAP inventory. In the "no transport" case, we turned off horizontal

Table 2. NMSE and Correlation Coefficient (R) of Anthropogenic NO_x Emissions Compared to True Emissions in Pseudo-observation Tests for Base Year (2010)

	σ_a = 0.5					σ_a = 1.5				
			Mass Balance					Mass Balance		
	Prior	4D-Var	W/o Kernel[a]	W/ Kernel[b]	Normal[c]	Prior	4D-Var	W/o Kernel[a]	W/ Kernel[b]	Normal[c]
NMSE	3.17	0.39	1.01	1.04	0.87	1.32	0.32	0.54	0.56	0.57
R	0.98	0.97	0.97	0.96	0.96	0.98	0.98	0.97	0.95	0.98

[a]Assuming lognormal distribution of emissions, without averaging kernel.
[b]Assuming lognormal distribution of emissions, with averaging kernel as described in equation A12.
[c]Assuming normal distribution of emissions, without averaging kernel.

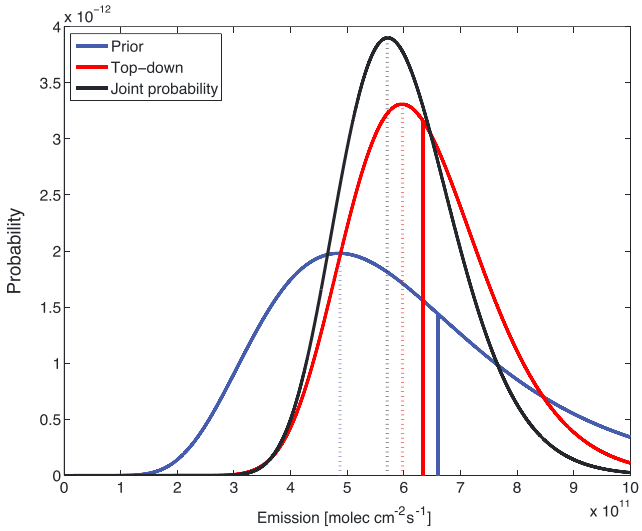

Figure 3. An example of a probability distribution function of the likelihood of being the true emissions given: prior emissions from bottom-up inventory (blue), top-down estimate by applying the ratio of observed column density (red), and their joint probability (black). The mean of each probability distribution function is shown as a solid vertical line in corresponding colors. The maximum likelihood emission value is shown as a dotted line. The emission corresponding to the maximum likelihood estimation of the joint probability is the posterior of the mass balance method we use in this study.

transport of all species across model columns. In order to avoid model crashes owing to accumulation of tracer concentrations when chemistry is turned off, we only allow emissions at the first time step for "no chemistry" cases. For these tests, we only use top-down emissions calculated from equation (A1) to estimate a new slant column density; we do not include a weighted balance between prior and posterior emissions (equation (A9)), as the goal for these cases is to see how well the model can match the observations, rather than to estimate physically meaningful emissions. We then evaluate correlations between model estimates of NO_2 slant column density and observations from OMI for the following cases: (a) prior model estimates before inversions, (b) posterior with chemistry and transport on, (c) posterior without chemistry and transport, (d) posterior without chemistry, with transport, and without averaging kernel, (e) posterior without chemistry, with transport and averaging kernel, and (f) posterior without transport, with chemistry. These are shown in Figure 4. Without chemistry and transport, the column density simulated by GEOS-Chem has increased by exactly the same ratio as applied to emissions, and thus the posterior simulation is a near-perfect match to the observations. With only chemistry, the posterior column density and OMI observations have a correlation of 0.95. Simulations with only transport lead to lower correlations of 0.90 (without averaging kernel) and 0.83 (with averaging kernel), suggesting that use of an averaging kernel (see equation (A11)) does not improve the posterior simulation. When both chemistry and transport are turned on, the normalized mean bias (NMB) after applying mass balance without using an averaging kernel is 9.2%, smaller than when applying mass balance with an averaging kernel (10.5%), although correlation coefficients are the same in both cases. In more realistic settings, the performance of mass balance inversions may be different at different length scales, may vary from time to time, and may be improved through more sophisticated approaches [e.g., *Toenges Schuller et al.*, 2006; *Boersma et al.*, 2008; *Lamsal et al.*, 2011; *Ghude et al.*, 2013], but overall, in the absence of any restrictions on emissions from prior information, we find that the ability of simple mass balance inversions to improve 16 days' simulated NO_2 SCDs at the 0.5° × 0.667° resolution is limited both by chemistry and not explicitly accounting for transport of NO_x emitted from neighboring grid cells when ascribing differences in simulated and observed NO_2 column densities to emissions.

3.2.2. Evaluation Using Pseudo-Observations

Mass balance emission scaling factors are evaluated using pseudo-observations generated with the same setup as described in section 3.1.2. Figure S2 shows posterior emission scaling factors with and without averaging kernel, i.e., use equation (A13) and (A1) for E_t in equation (A9), in the cases of $\boldsymbol{\sigma_a}$ = 0.5 and $\boldsymbol{\sigma_a}$ = 1.5. There are more overcorrection of emissions in the case of $\boldsymbol{\sigma_a}$ = 1.5 than in the case of $\boldsymbol{\sigma_a}$ = 0.5, which can also be explained by the weighting of observation error in the maximum likelihood estimation. This preferential change of emissions with lower uncertainty causes reduction of overestimates rather than reduction of underestimates and leads to a negative bias after mass balance inversions. More details of these tests are in the supporting information.

NMSE and correlation coefficient of the mass balance posterior emissions obtained with and without an averaging kernel, and their comparisons with posterior emissions obtained with the assumption of normally distributed emissions are shown in Table 2. Posteriors in these three cases have very similar NMSE and

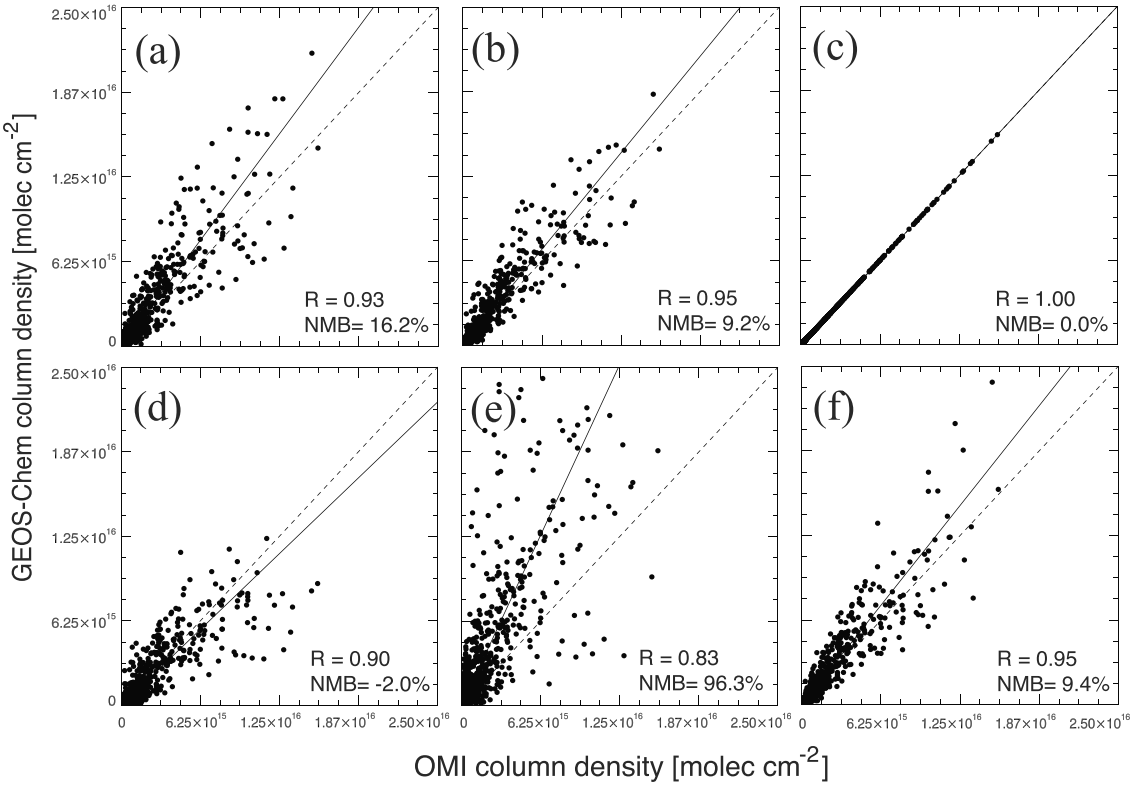

Figure 4. Correlation of OMI and GEOS-Chem NO_2 slant column densities in a half-month simulation from 1–16 January 2010. GEOS-Chem simulations are run with (a) bottom-up emissions, with chemistry and transport on, (b) posterior from mass balance with chemistry and transport on, (c) posterior from mass balance with no chemistry or transport, (d) posterior from mass balance with no chemistry, transport on, and no averaging kernel, (e) posterior from mass balance with no chemistry, transport on, and averaging kernel applied, and (f) posterior from mass balance with transport off but chemistry on. The solid line is a linear fit, and the dashed line is the 1:1 line.

correlation coefficients. This suggests that the assumption of either normally or lognormally distributed emissions does not much affect the performance of mass balance inversion. However, the way the averaging kernel is applied may not fully capture the true processes in chemical transport. In reality, the monthly average wind is less likely to blow uniformly from all directions. Therefore, accounting for transport by an averaging kernel that has equal weight in all directions may not be suitable. One possible way to improve this could be weighting contributions from surrounding grid cells by wind directions. We assume lognormal distribution of emissions, and leave out the averaging kernel in this study based on the following: imbalanced behavior of the kernel when increasing and decreasing emissions, occasional negative emissions resulting from the case of $r < 1$ in equation (A13) (r is the ratio of SCD_{obs} to SCD_{GC}) when the weight of changes in emissions considering transport from adjacent cell (w) is large, and very similar performance of the mass balance inversion in all these three cases.

3.3. Comparison of 4D-Var and Mass Balance Approach

From Table 2, the NMSE of the 4D-Var posterior is 61% ($\sigma_a = 0.5$) and 41% ($\sigma_a = 1.5$) smaller than the NMSE of the mass balance posterior (assuming lognormal distribution, without averaging kernel). However, in another set of pseudo-observation tests without introducing noise in the initial guess, the NMSE of the mass balance posterior are less different (<25%) than that of 4D-Var with off-diagonal error covariance matrix. This difference is even smaller when compared to 4D-Var with diagonal error covariance matrix (5.8% larger when the initial guess is low and is the same with 4D-Var using diagonal $\mathbf{S_a}$ when the initial guess is high). This much better performance of 4D-Var after introducing noise to the initial guess can be explained by its strength in correcting the spatial distribution of emissions. Nevertheless, 4D-Var inversion has much higher computational cost than mass balance (it takes about 2 weeks of wall time for the 4D-Var approach on a dual hex-core 2.6 GHz server, whereas the mass balance approach requires only a forward model run that takes about 12 h on the same system). Therefore, a more effective inversion approach is needed to derive long-term emissions with more accuracy.

3.4. Hybrid Approach

Here we seek a way to combine the performance of the 4D-Var approach (with off-diagonal $\mathbf{S_a}$) with the low computational cost of the mass balance approach to facilitate decadal-scale inversions. We consider two types of hybrid approaches.

In one hybrid approach, scaling factors derived from the mass balance equation are calculated first. These scaling factors and errors are then used as the initial guess for the 4D-Var approach. Using the same setup as the pseudo-observation test described in section 3.1.2, we find that this hybrid approach requires more iterations for the cost function to converge to the same value obtained using the 4D-Var approach alone. This is mainly caused by the overcorrection and undercorrection of mass balance scaling factors, which leads to emissions that are spatially less smooth and incur a larger parameter error. For instance, in the case of $\sigma_a = 0.5$, the parameter error in this hybrid inversion is 15,359, making up 51% of the cost function in the first iteration and decreases to 235, 7% of the cost function when it converges in the 48th iteration, whereas in 4D-Var alone, the value of the parameter term is 0 in the first iteration and 682, 18% of total cost function in the eighteenth iteration when it converged. It takes more iterations for the off-diagonal term in 4D-Var to smooth the initial condition in the hybrid inversion, since mass balance emission scaling factors are not spatially correlated. Therefore, even if the cost function in the first iteration of this hybrid approach is less than half of that in standard 4D-Var, it subsequently decreases at a much slower rate considering the less smooth initial emissions.

Another way to combine these two approaches to speed up monthly-scale inversions for an entire decade is to first perform a 4D-Var inversion for a particular base year, and use this as a basis for mass balance inversions in other years. The purpose of this first step is to correct for the spatial distribution of emissions and decrease the systematic error from the bottom-up emission inventory. Given that differences of NO_2 column densities from OMI and GEOS-Chem simulation have very similar monthly differences on an interannual basis in our studied domain, the optimized emissions from the 4D-Var approach in the base year are used as the prior emissions for other different years' mass balance inversion. Here we also validate this hybrid method by setting up pseudo-observation tests. Optimized emission scaling factors from the 4D-Var approach in the pseudo-observation test (section 3.1.2) are used as the 4D-Var solution for the base year (2010). Additional sets of pseudo-observations are generated for January in other years using adjusted true emissions, i.e., 0.6 times the true emissions in the base year are used as true emissions for 2006, 0.7 times for 2007, 0.8 times for 2008, 0.9 times for 2009, 1.1 times for 2011, and 1.2 times for 2011. This means adjusting true emissions and corresponding pseudo-observations a little bit, as they would be expected to change from year to year [*Liu et al.*, 2016]. Optimized emissions in base year is used to simulate column densities in January for other years. Further inversion from mass balance is applied by scaling the optimized emission in 2010 by the ratio of the NO_2 column densities from pseudo-observations in corresponding month and the NO_2 column densities in the previous simulations. We assume same emission change rate for all NO_x sources and apply the same ratio to all NO_x emission sectors in mass balance inversion. The distribution of NO_x emissions is assumed to be lognormal in the mass balance constraint but normal in the 4D-var inversion. A lognormal assumption of emission scaling factor is more physically realistic, since it does not allow for negative emissions [*Henze et al.*, 2009]. However, in a 4D-Var inversion, log scaling factors cannot increase emissions as efficiently as linear scaling factors and would lead to a solution that deviates more from the true state than the solution using linear scaling factor [*Jiang et al.*, 2015]. Though this is somehow inconsistent, the performance of hybrid inversion with this setting is found to be better than uniformly using either lognormal or normal distribution in 4D-Var and mass balance.

We examine the effectiveness of this hybrid approach in two ways. In Table 3, the NMSE of the optimized emissions compared to true emissions in each year's hybrid inversions are compared with that using mass balance in each year and to that using 4D-Var just in 2010. For the case of $\sigma_a = 1.5$, emissions optimized with the hybrid approach have smaller NMSE (by 59% to 78%) than mass balance posterior emissions in all studied years. This suggests that posterior emissions of the hybrid inversion deviate less from the true emissions than the posterior mass balance emissions. For the case of $\sigma_a = 0.5$, initial emission in 2006 and 2007 are very close to the true state. Under such circumstances, further inversion would increase error of emissions. Also, applying 4D-Var scaling factor from 2010 leads to further deviation from the true emissions. Therefore, mass balance posterior emissions in these two years have smaller NMSE than that of hybrid posterior. In 2008, 2009, 2011, and 2012, when initial guesses deviate more from the true emissions, the hybrid inversion is more effective in decreasing the error, and therefore has smaller NMSE than the mass balance posterior.

Table 3. NMSE of Anthropogenic NO_x Emissions for 2005–2012 in Pseudo-observation Tests

		$\sigma_a = 0.5$				$\sigma_a = 1.5$			
		Prior	4D-Var (2010)	Hybrid	MB	Prior	4D-Var (2010)	Hybrid	MB
NMSE	2006	0.36	1.68	0.62	0.19	6.05	2.64	1.48	3.63
	2007	0.83	0.90	0.25	0.20	4.18	1.60	0.74	2.11
	2008	1.50	0.50	0.28	0.48	2.89	0.94	0.49	2.12
	2009	2.29	0.36	0.27	0.65	1.97	0.54	0.32	1.47
	2010	3.17	0.39	0.46	1.01	1.32	0.32	0.33	0.54
	2011	4.12	0.55	0.47	1.67	0.86	0.24	0.24	1.10
	2012	5.12	0.80	0.57	2.14	0.54	0.25	0.20	0.54

We also evaluate how similar the posterior time series is compared to the true emissions. In Figure 5, the time series of the total emissions in the hybrid approach ($R = 0.991$ for $\sigma_a = 0.5$, $R = 0.983$ for $\sigma_a = 1.5$) has a better correlation than that of the mass balance approach ($R = 0.914$ for $\sigma_a = 0.5$, $R = 0.965$ for $\sigma_a = 1.5$). While we find that correlation coefficients of the hybrid posteriors are larger than that of mass balance in both cases, the difference between them is statistically significant at the 95% confidence level for the $\sigma_a = 0.5$ case, but not for the $\sigma_a = 1.5$ case. Correlations of the hybrid inversion are worse if not further applying mass balance to the 2010 emissions. However, to avoid using the same observations twice in the inversion, in the following real observation simulations all reported hybrid posterior in 2010 are just based on a 4D-Var inversion. Our posterior underestimates NO_x emissions in most years for both $\sigma_a = 0.5$ and $\sigma_a = 1.5$. This can be explained by the combined effects of preferentially decreasing emissions for 4D-Var and mass balance as described in sections 3.1.2 and 3.2.2. In addition, there are fewer observations from OMI in 2011 and 2012, and therefore, the mass balance step can hardly change emissions from 2010 levels in the hybrid inversion. Overall, the growth rate of hybrid posterior (40.4% for $\sigma_a = 0.5$ and 39.8% for $\sigma_a = 1.5$) is smaller than that of true emissions (100% for both cases) from 2006 to 2012, compared to a 44.3% growth rate of true NO_2 column densities, a 15.3% increase for $\sigma_a = 0.5$, and a 14.0% increase for $\sigma_a = 1.5$. The growth rate of mass balance posterior is even smaller, with a growth rate of 34.7% for $\sigma_a = 0.5$ and 37.8% for $\sigma_a = 1.5$. The magnitude of changes in NO_2 column densities is smaller than that of NO_x emissions, because column density is affected by meteorology even with constant emissions and changes nonlinearly with different emissions under constant meteorology fields. The smaller growth rate of the posterior emissions compared to the true emissions can be attributed to three causes. First, in our Bayesian analysis, the posterior emissions are restricted by the value of the prior emissions and their uncertainties. When these uncertainties are increased (magenta lines in Figure 5a, which have the same observation errors as the mass balance and hybrid inversions but 100% uncertainty in prior emissions),

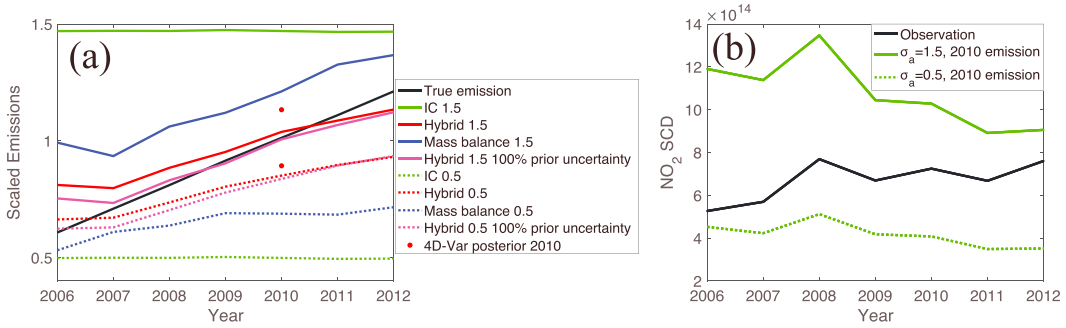

Figure 5. (a) Time series of prior, posterior, and true emissions for all NO_x sources in the pseudo-observation tests. Scaled emissions are calculated as the ratio of emissions to the true emissions in 2010. Monthly pseudo-observations are generated for January 2006–2012. Hybrid inversions are performed by first applying the 4D-Var scaling factor from January 2010 to other years, followed by mass balance inversion. The black line shows the true emissions; the green lines are the prior emissions; the red and blue lines are the posterior emissions from the hybrid and mass balance inversions, respectively. The two red dots are 4D-Var posterior emissions in 2010, with the larger value for $\sigma_a = 1.5$ case. The solid and dotted lines show results for $\sigma_a = 0.5$ and $\sigma_a = 1.5$, respectively. (b) Time series of monthly average NO_2 SCD over China. The black line is the trend of pseudo-observations simulated with the true emissions. The green lines are NO_2 SCD simulated using constant prior anthropogenic emissions in 2010.

the posterior emissions trend is improved. Second, due to the impacts of meteorology, NO_2 columns for simulations with constant (2010) anthropogenic emissions (Figure 5b) themselves have a trend opposite that of the emission trends in our pseudo inversions. This opposing relationship between emissions and column concentrations serves to reduce the increasing trend in the posterior emissions. Third, the quality and density of observations are not uniform throughout the time frame. When there are fewer observations, the hybrid posterior emissions tend toward the value of the 4D-Var 2010 posterior emissions, leading to smaller deviations from 2010 emissions compared to the true emissions. This is particularly apparent in 2006 when there are very few observations in central East China, so the sum of emission over China has almost the same value in 2006 and 2007. These evaluations show the ability of the hybrid inversion to detect variability of NO_x emissions over several years. They also highlight the potentially different trends of NO_x emissions and NO_2 columns, which will also occur when using real observations from OMI in section 4.2.

4. Long-Term Hybrid Inversion with Real Observations

4.1. 4D-Var Inversion in Base Year

We choose 2010 as the base year for hybrid inversion and perform adjoint-based 4D-Var inversions for each of the 12 months in this year. Comparisons of adjoint forcing, which is the difference between predicted and observed column density weighted by observation errors before and after inversions are shown in Figure 6. Changes mostly occur in regions that have strong positive forcing, especially in the areas outlined by the black rectangle. Column density predicted by GEOS-Chem using prior and posterior emissions and that observed by OMI in January, April, July, and October of 2010 are shown in Figure 7. The optimized emissions generally decrease simulated NO_2 column densities in China, especially inside the black rectangular area in each month. This leads to an increase of negative bias in posterior NO_2 column densities, when compared to OMI observations. In July and other summer months, the spatial distribution and total amount of predicted NO_2 column densities from GEOS-Chem are quite similar to those of OMI observations, even before any inversion. Therefore, after inversion, correlations of predicted NO_2 column densities stay the same for July, but have been improved for January, April, and October. A preference in the L-BFGS-B optimization algorithm to decrease emissions has been noticed previously, due to the asymmetry of emission scaling factors distributed around 1.0 and bounded on one side at 0.0, but unbounded in the other direction. Following *Wells et al.* [2015], we impose an upper bound of 5 on the scaling factors. The asymmetric behavior is further influenced by asymmetries in the observation errors. The minimization procedure tends to change emission in grid cells where concentrations are high, uncertainties of satellite observations are small, and adjoint forcings are large. This behavior can be clearly seen from Figure 6, in which adjoint forcing in East China has decreased significantly, whereas column densities in places with larger observation uncertainties (e.g., over the ocean) and smaller adjoint forcing remain essentially unchanged after the inversion. This preferentially leads to reduction of overestimates rather than reduction of underestimates and therefore results in more negative NMB after inversions.

4.2. Long-Term Inversion

We use optimized emissions from 4D-Var inversions in each month of 2010 as prior emissions for the corresponding months of other years from 2005 to 2012. Mass balance inversions are then performed to obtain posterior emissions throughout the decade. There is a similar preferentially decreasing behavior in emissions here using real OMI observations with mass balance inversion, as is described and explained in section 3.2.2.

Trends of NO_2 columns from GEOS-Chem simulations and OMI observations are shown in Figure 8. We compare optimized NO_2 columns from three inversion methods (mass balance, 4D-Var in 2010, and hybrid) with prior simulations over the whole of China, major economic regions (Beijing municipality, Yangtze Delta Area, Guangdong province, and Beijing-Tianjin-Hebei), and some provinces in western China. After the hybrid inversion, the simulated NO_2 column over China has significantly better correlation with OMI observation than that after mass balance inversion ($R = 0.948$ versus $R = 0.911$). In other studied regions, the difference in the posterior correlation between these two methods is within the range of 0.05. In contrast to the initial simulation, NO_2 columns after the hybrid inversion over China rise from 2005 to 2012 by 9%. A generally increasing trend on this 8 year scale is seen in some economic regions (e.g., Beijing municipality and Yangtze River Delta), Inner Mongolia Autonomous Region, and several provinces in Western China (e.g., Xinjiang, Ningxia, Qinghai, Shaanxi, and Gansu). However, decreases of NO_2 columns of 11–39% occur in the following provinces: Guangdong, Chongqing, Guizhou, Sichuan, and Guangxi. Optimized column densities generally have lower values than the initial state. This can be explained by the weighting of errors, which preferentially

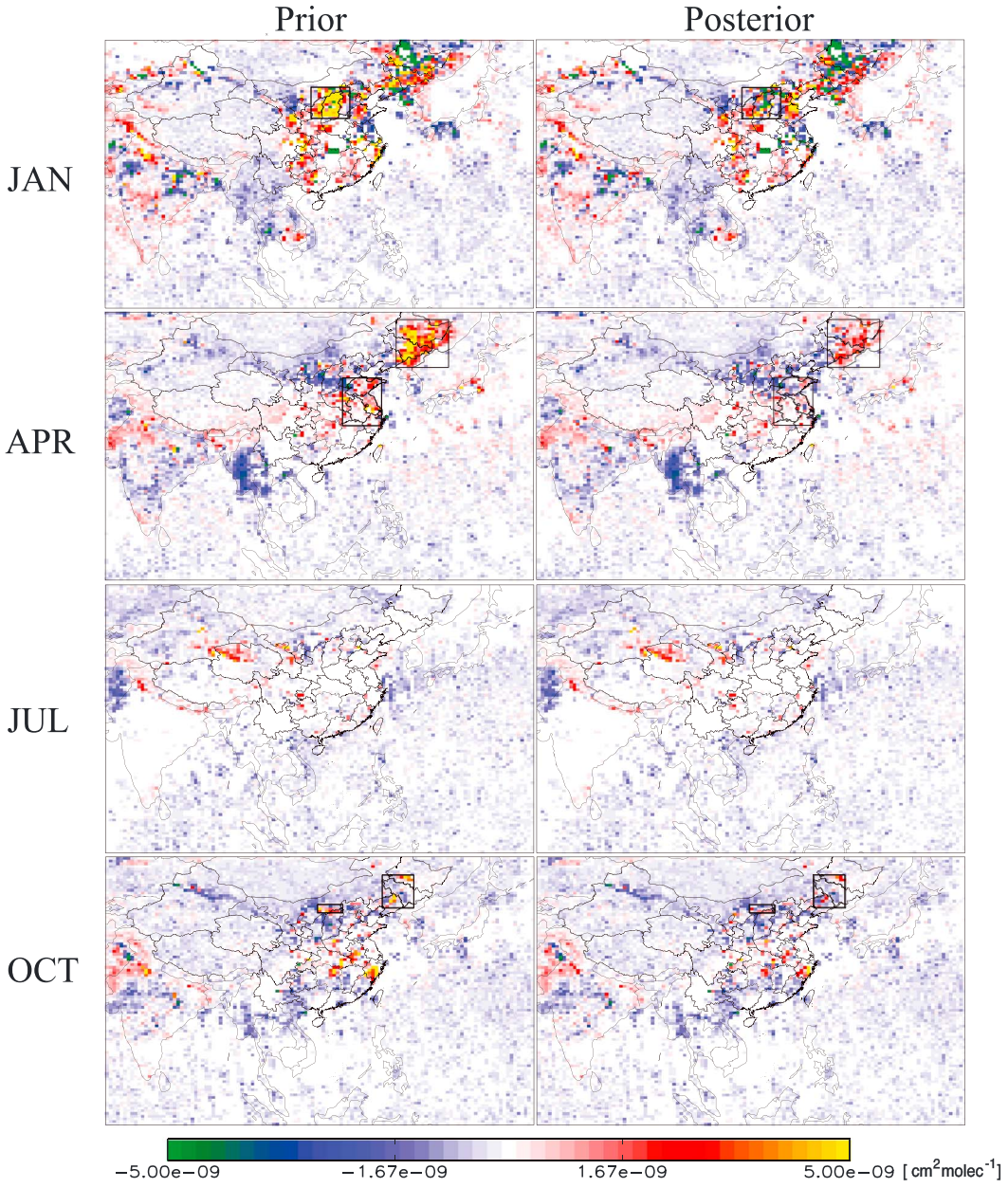

Figure 6. Adjoint forcing in January, April, July, and October of 2010, for the prior and posterior 4D-Var inversion. The adjoint forcing is the sum of the difference between observed and simulated NO_2 column densities weighted by the inverse of observational error covariance.

leads to reduction of overestimates rather than reduction of underestimates, as discussed in section 3.4. It is hard for the inversion to increase NO_2 column density in regions where initial column densities are much lower than observations from OMI (e.g., Xinjiang Province, Qinghai Province, and Yunnan Province). Also, since we set an absolute uncertainty of 10^{15} molecules cm^{-2} for each individual observation in the 4D-Var inversion, and a lower limit of 1.5×10^{15} molecules cm^{-2} in the mass balance inversion, locations with smaller column densities than these two values hardly exhibit changed emissions after the optimization. In locations without satellite observations, it is also difficult to improve emissions.

Trends in OMI NO_2 retrievals at regional scales may be susceptible to biases in the retrieval process itself [e.g., *Herron-Thorpe et al.*, 2010; *Zheng et al.*, 2014; *Ialongo et al.*, 2016]. To test the robustness of the trends driving our inversion, we next compare the two retrievals of OMI NO_2 product here. We find that the annual mean values of the OMI NO_2 columns from NASA standard product are generally smaller (by ~50%) than that from

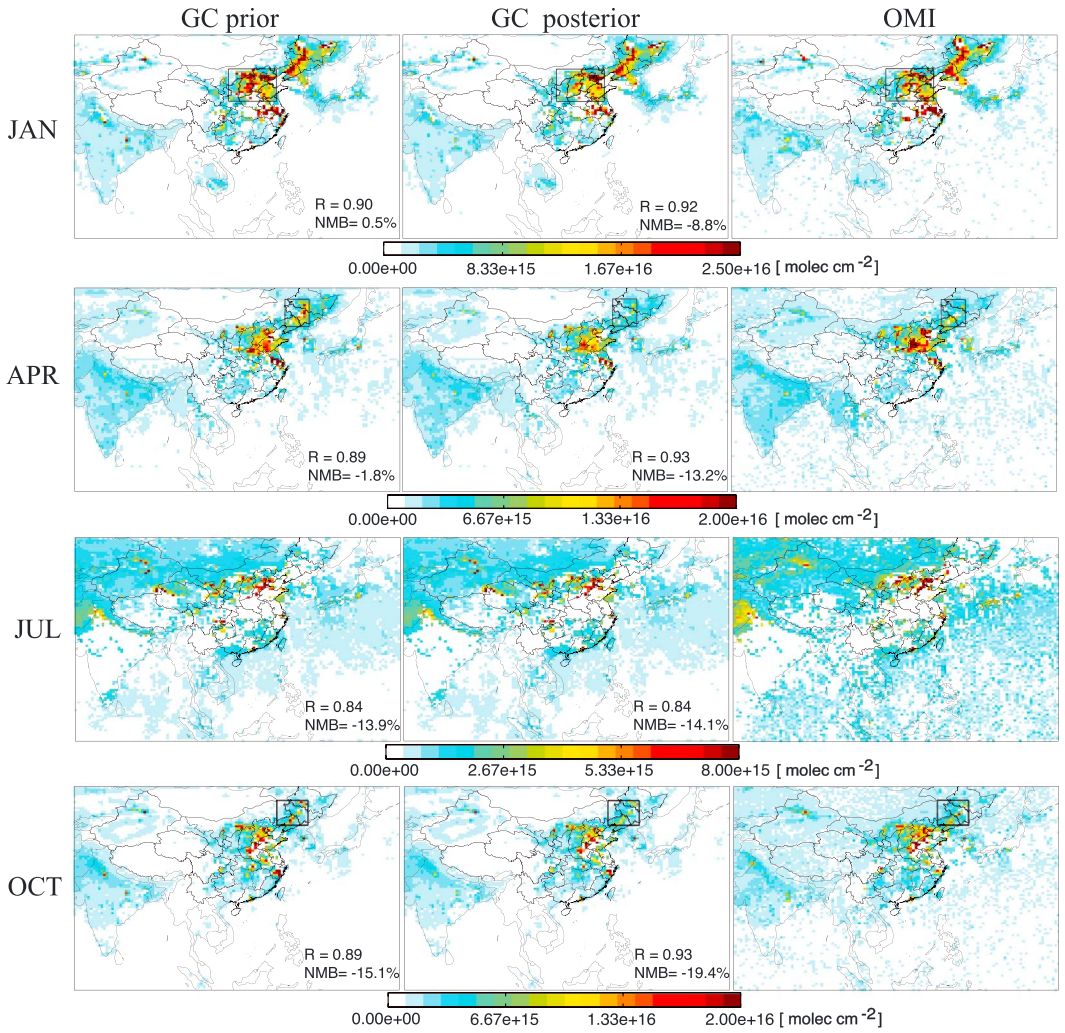

Figure 7. NO_2 slant column density in January, April, July, and October of 2010. The first two columns are predicted column density with prior emissions from HTAP and posterior emissions from 4D-Var inversions. The third column shows NO_2 slant column density from OMI.

the DOMINO product in densely populated and industrial regions. This discrepancy is consistent with previous comparisons of these two products over this region [e.g., *Zheng et al.*, 2014]. In Figure 8, we compare the annual mean from these two products at the regional scale. The correlation coefficients of these two trends are negative in Chongqing, Guizhou, Sichuan, and Guangxi, but are above 0.6 in mainland China, Beijing, the Yangtze River Delta, Xinjiang, Shaanxi, Qinghai, Gansu, Ningxia, and Inner Mongolia, suggesting that trends of NO_2 columns in the latter regions are more robust. Correspondingly, NO_x posterior emissions are likely less affected by differences in NO_2 retrievals in these regions.

Finally, to evaluate the impact of data availability reduced by row anomalies on the NASA standard OMI retrievals, we consider the approach of *Duncan et al.* [2013] and use the trend in NO_2 columns from only rows 10 to 23, which are unaffected by row anomalies throughout the period. As shown in the grey lines in Figure 8, these values are mostly lower than those using observations from all rows, but the two time series are quite well correlated ($R > 0.75$) except for Guangxi, Sichuan and Chongqing. For deriving top-down emissions, we chose to use all observations available after data filtering, but recognize that the inferred trends are most robust (both R_DOMINO and R_row are larger than 0.9) with respect to the retrieval and processing steps in Yangtze River Delta, Xinjiang, Ningxia, and Inner Mongolia.

We compare total (including anthropogenic and natural sources) prior and posterior NO_x emissions in Figure 9. Even though hybrid and mass balance inversions have similar total posterior emissions, their spatial

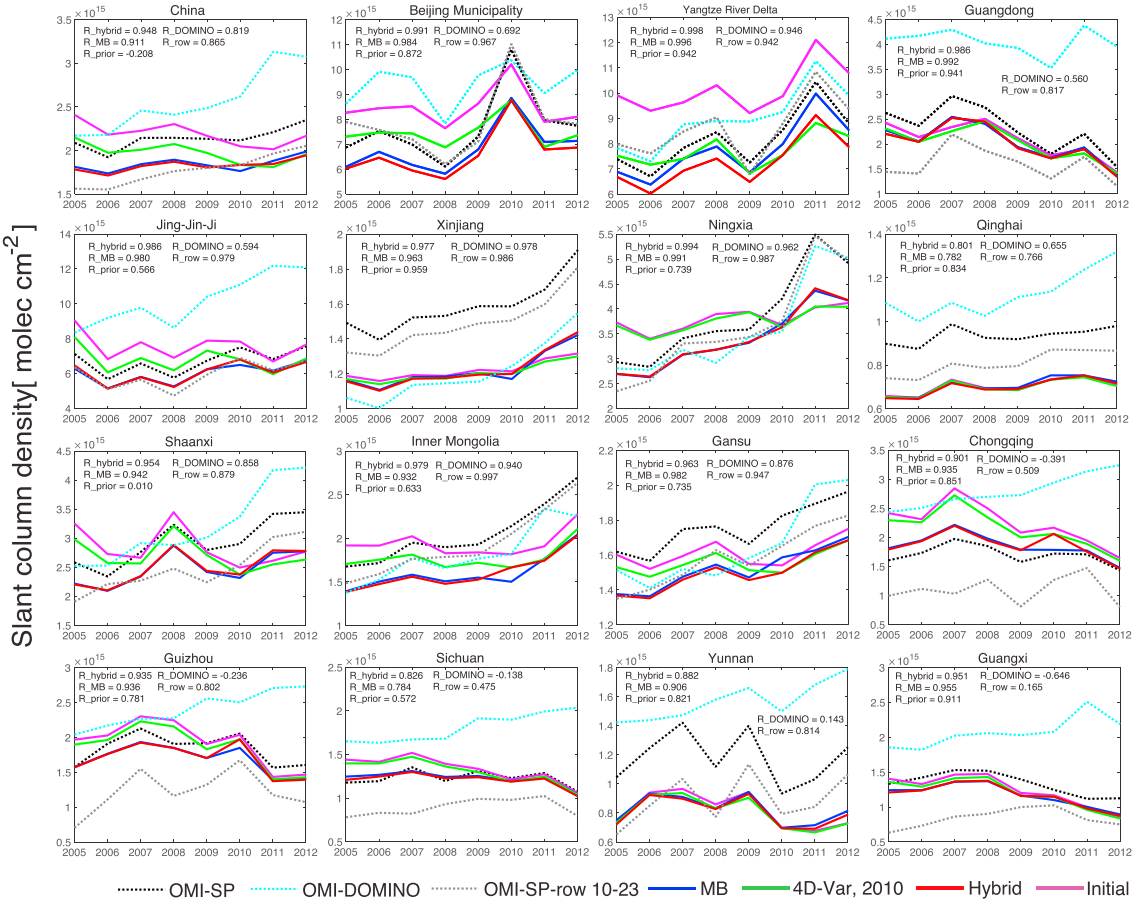

Figure 8. Annual averaged NO_2 SCD over the mainland China, major economic areas, and western China. The black dotted line is NO_2 column density from OMI using the NASA standard product; the cyan dotted line is OMI NO_2 columns from the DOMINO product; the grey dotted line is the NASA standard OMI NO_2 column only from row 10 to 23 throughout the 8 years; the magenta line is simulated column density with prior emissions; the green line is the modeled value with 4D-Var scaling factor from 2010 applied; the red and blue lines are the posterior from hybrid and mass balance inversions, respectively. We also show the correlation between the standard product SCD (black dotted) and the following: SCD simulated using hybrid posterior (*R*_hybrid); mass balance posterior (*R*_MB); constant HTAP emissions in 2010 (*R*_prior); the DOMINO product (*R*_DOMINO); and the standard product (with all data after filtering) using only rows 10 to 23 (*R*_row).

distribution can be very different. For instance, total posterior NO_x emissions in 2005 from the hybrid inversion is 6.63 Tg N yr^{-1} and that from the mass balance inversion is 6.59 Tg N yr^{-1}, but the grid-scale difference of the posterior emissions from these two can be as much as 100%, as shown in Figure 10. There are a few grid cells that have isolated negative values which coincide with locations with large emissions and overestimates from GEOS-Chem when compared to OMI observations. In these grid cells, when optimizing emissions using the mass balance method, only emissions in the local grid cell will decrease, whereas the 4D-Var approach spreads the decrease of emissions to surrounding grid cells through the off-diagonal error covariance matrix. Therefore, the emission in the local grid cell decreases more through mass balance than through 4D-Var approach, and consequently, the differences between posterior from these two are very negative in these grid cells.

Over China, optimized NO_x emissions are generally on the rise during the studied period, with small anomalies in 2008 and 2012. The decrease of NO_x emissions in 2008 (2% decrease compared to emissions in 2007) can be explained by economic recession and emission reduction measures during the Beijing Olympic Games period, as will be discussed in section 5.1. NO_x emissions in Beijing, as shown in Figure 9, are on the decline in 2007 (by 5.1%) and 2008 (by 3.6%), increase by 3.8% in 2009 and 18.1% in 2010, decrease by 4.9% in 2011, and stay almost the same in 2012. In the Yangtze River Delta Economic Zone, NO_x emissions are generally on the rise (by 0.6–9.5%), with small (<4.4%) decreases in 2006, 2008, and 2012. NO_x emissions in Guangdong Province fluctuate more during this period, with an increase (by 6.6%) in 2007 and decreases in 2008 (by 9.1%)

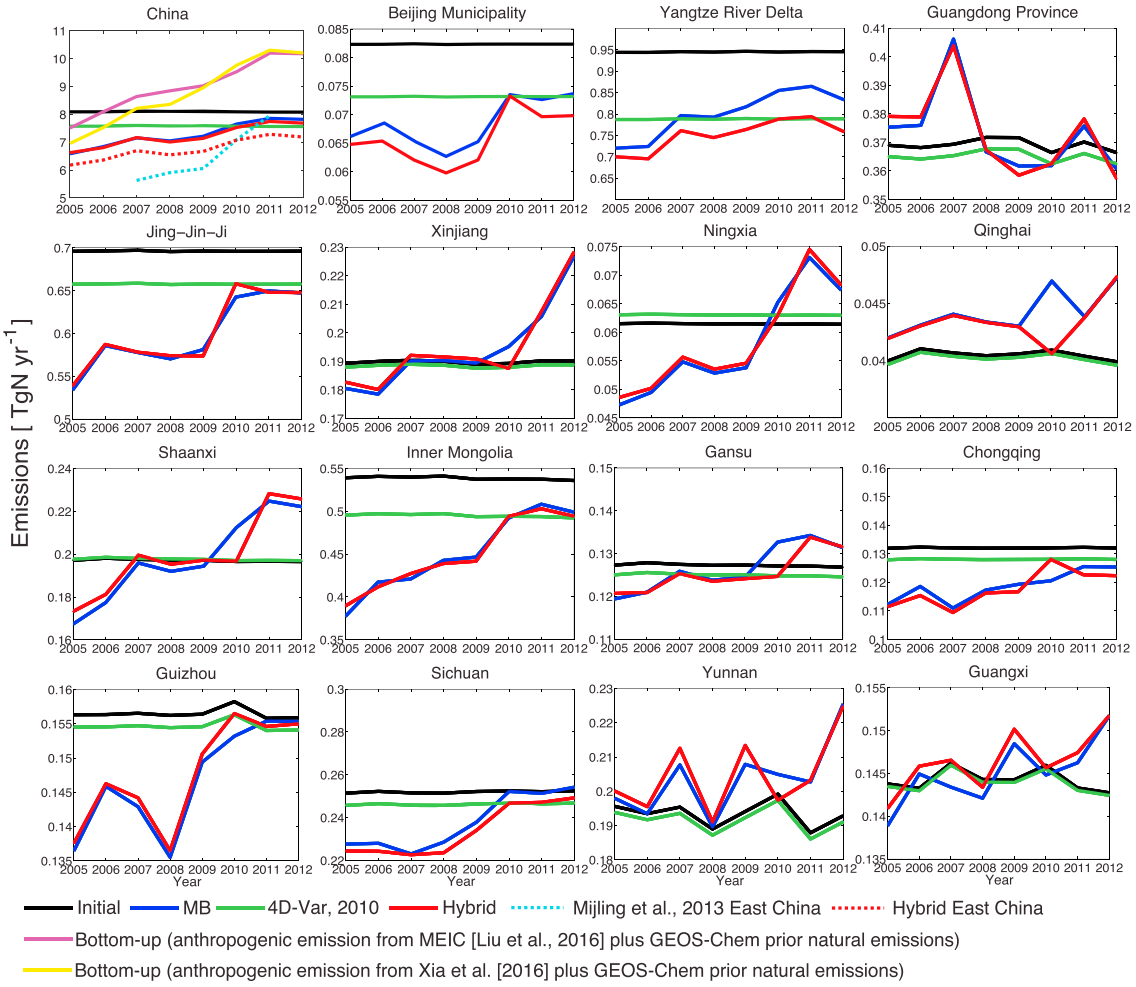

Figure 9. The sum of NO_x emissions from all sectors over the mainland China, major economic areas, and western China. The black line is prior emissions (both anthropogenic and natural sources); the green line is emissions calculated by applying 4D-Var scaling factor in 2010; the red and blue lines are posterior from hybrid and mass balance inversions, respectively. In the first panel, the red dotted line is the hybrid posterior emissions over East China (18–50°N, 102–132°E); the magenta line in the first panel is the bottom-up anthropogenic emissions from the MEIC inventory plus GEOS-Chem prior natural emissions; the yellow line is the bottom-up anthropogenic emissions from *Xia et al.* [2016] plus GEOS-Chem prior natural emissions. The cyan dotted line in the first panel is the top-down estimate for total emissions in East China (18–50°N, 102–132°E) from *Mijling et al.* [2013].

and 2012 (by 5.5%). Fluctuations of posterior emissions in years other than 2007, 2008, and 2012 during the study period are about 0.1% to 4.3% compared to each previous year. Emissions in provinces in Western China are generally on the rise during the studied period, even though NO_2 column densities are decreasing in some of these provinces. Possible causes for opposing trends in NO_x emissions versus NO_2 columns are discussed later.

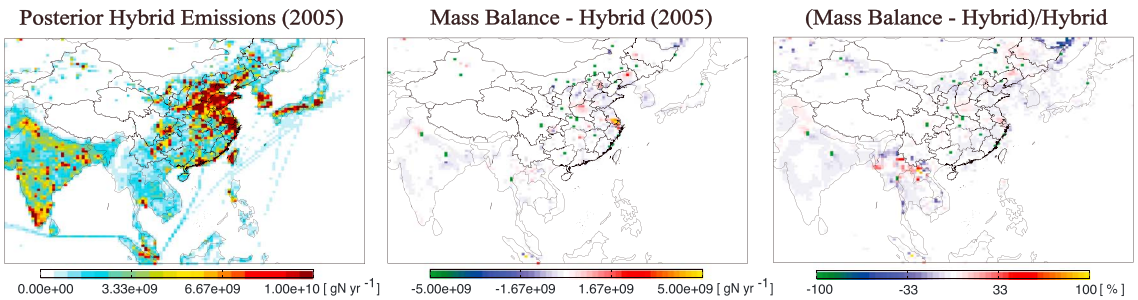

Figure 10. Difference of posterior annual budget of NO_x emissions in 2005 from hybrid and mass balance inversions.

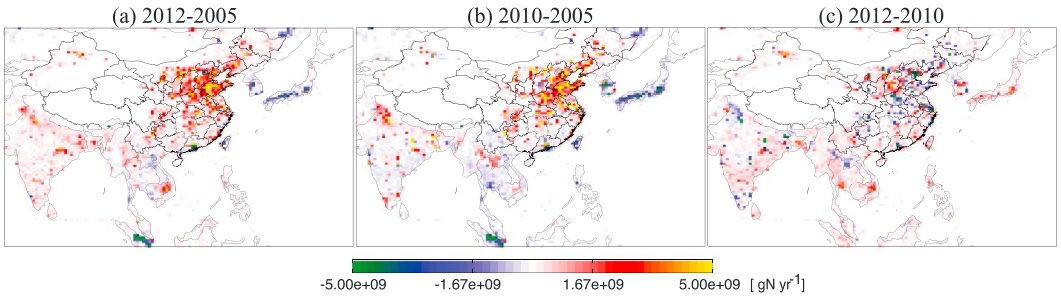

Figure 11. Spatial distribution of changes in total annual NO_x hybrid posterior emissions from (a) 2005 to 2012, (b) 2005 to 2010, and (c) 2010 to 2012. The black rectangle in Figure 11a indicates the Mentougou district, which has a different trend from the whole city of Beijing.

Changes in the emissions from the hybrid inversion from 2005 to 2012 are shown in Figure 11a. NO_x emissions are generally on the rise in most parts of China, but decreases are found in Mentougou district of Beijing (3.1×10^6 kg N yr^{-1}, 12%), the urban center of Guangzhou (6.5×10^6 kg N yr^{-1}, 10%), Shenzhen (9.3×10^6 kg N yr^{-1}, 18%), Zhuhai (6.5×10^6 kg N yr^{-1}, 26%), Hong Kong (9.3×10^6 kg N yr^{-1}, 18%), and Macau (2.7×10^6 kg N yr^{-1}, 25%), which are major industrial and economic areas. NO_x emissions in the rest of East China, however, generally increase by more than 1.0×10^6 kg N yr^{-1} per grid cell in the GEOS-Chem 0.5° × 0.667° resolution, as shown in Figure 11a. As we have seen in Figure 9, total NO_x emissions in Yunnan Province almost stay the same in 2005 and 2010, but from Figure 11b, there are actually some areas which have increased emissions (e.g., Kunming, the largest city in Yunnan Province) and some areas which have decreased emissions (e.g., Pu'er Prefecture). From 2005 to 2010, decreases of NO_x emissions are seen in large areas of Yunnan Province, Guangdong Province, Fujian Province, and Jiangxi Province (Figure 11b). Since 2011, more decreases (compared to 2010) are detected in Beijing, Tianjin, Hebei Province, Henan Province, Shandong Province, Hubei Province, and Pearl River Delta area (Figure 11c). These suggest effective pollution control measures in these regions during China's eleventh "Five Year Plan" (2006–2010) and twelfth "Five Year Plan" (2011–2015), which specified for the first time a commitment to reduce NO_x emissions by 10%.

In addition to changes in NO_x emissions, trends in NO_2 columns can be influenced by meteorology. In Figure 8, initial NO_2 column densities (magenta line) are simulated with the same anthropogenic emissions and only slightly different natural emissions (as shown in Figure 1) over the whole period (the sum of emissions from all sectors are shown in black in Figure 9), but over China, meteorology is found to cause a 9.3% decrease in 2006 and a 7.7% increase in 2012 even though NO_x emissions actually increase from 2005 to 2006 and decrease from 2011 to 2012. Similar behavior is also seen in other years and in other studied regions. The maximum magnitude of meteorological contribution to annual changes in NO_2 columns ranges from 6.0% (in Xinjiang) to 29.6% (in Guizhou). This influence from meteorology leads to different trends of NO_2 columns and trends of NO_x emissions, suggesting that studies looking at trends in NO_2 column densities without accounting for physical processes like transport, chemistry, and meteorology may incorrectly imply trends of NO_x emissions.

Besides differences in trends, posterior NO_x emissions also have changes that can be different in magnitude from changes in posterior NO_2 columns from 2005 to 2012, as we have seen in the pseudo-observation test in section 3.4. A comparison of NO_2 column changes and NO_x emission changes in major cities is shown in Table 4. In the urban center of Xi'an, Qingdao, Quanzhou, and Taipei, changes in NO_x emissions are about 1 order of magnitude different from changes in NO_2 columns. In the urban center of Tianjin, Fuzhou, Hangzhou, Suzhou, and Shanghai, NO_x emissions have increased from 2005 to 2012, but NO_2 columns show a decreasing trend. However, a decreasing trend can be found in surrounding grid cells except for Hangzhou, Suzhou, and Shanghai. This further shows the influence of atmospheric transport; scaling emissions based on local column density may not be able to catch the correct trend in emissions.

The seasonality of total NO_x emissions and that of natural and anthropogenic contributions are shown in Figures 12 and 13. In grid cells dominated by anthropogenic emissions, where contribution from anthropogenic sources represents more than 90% of the sum of emissions from all sectors in that grid cell, the peak of total NO_x emissions occurs in winter, when heating leads to increased combustion and emissions. In places dominated by natural emissions, where contribution from natural sources are more than 90% of the sum of emissions from all sectors in that grid cell, the peak of total NO_x emissions occurs in the summer, when higher

Table 4. Percentage Change of NO_x Emissions and NO_2 Column Densities From 2005 to 2012 in Major Cities (Compared to 2005 Level)[a]

City	NO_x Emission (%)	NO_2 Column Density (%)
Emissions and Column Densities Change in the Same Direction		
Beijing	15.96	4.66
Wuhan	45.28	12.25
Xi'an	53.03	2.09
Zhengzhou	29.62	17.05
Dalian	47.59	14.43
Shenyang	40.91	52.50
Quanzhou	23.87	1.13
Emissions and Column Densities Change in Different Direction		
Tianjin	39.17	−43.49
Fuzhou	22.24	−32.25
Hangzhou	12.92	−20.21
Suzhou	3.00	−35.72
Shanghai	19.49	−32.67
Qingdao	29.04	−1.68

[a]Changes of emissions and column densities are calculated at the single grid cell located at the center of each city.

temperatures lead to more emissions from soil and fertilizer, and lightning occurs more often. Overall, the summertime peak of total NO_x emissions (Figure 12) is dominated by contributions from natural sources.

5. Posterior Evaluations

5.1. Emission Reductions During Beijing Olympic Games

To test the ability of our hybrid inversion to detect variability and trends in NO_x emissions, we evaluate NO_x emissions during the Beijing Olympic Games and Paralympic Games period (July to October 2008) and compare them to emissions in other years (Figure 14). NO_x emissions decrease in Beijing (10–30%) and the surrounding provinces (2–14%) starting from 1 month before the Beijing Olympic Games (July) and lasting until 1 month after the Beijing Paralympic Games (October). These decreases can be explained by the several pollution control strategies implemented during the Beijing Olympic (8–24 August) and Paralympic (6–17 September) Games, when road space rationing and prohibition of vehicles not meeting standards led to a 46% reduction of NO_x emissions from mobile source [*Wang et al.*, 2010], and power plants were required to reduce their emissions by 30% from June levels. Several heavily polluting factories as well as all construction activities were also temporarily ceased during this period.

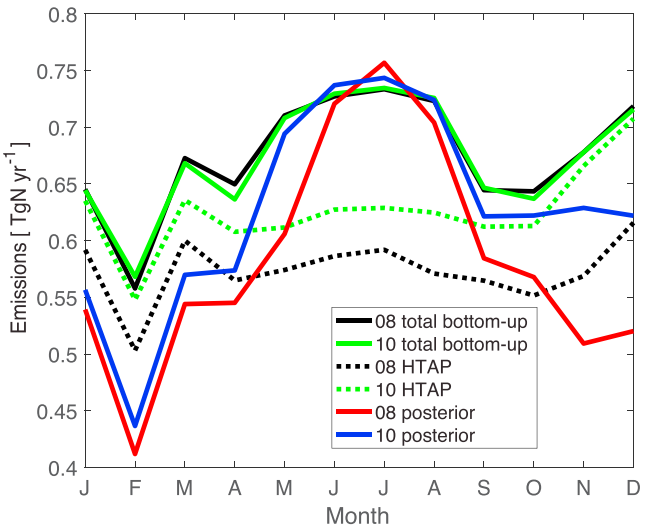

Figure 12. Comparison of monthly total posterior NO_x emissions from the hybrid inversion with the sum from bottom-up inventories for all sectors. The black and green dotted lines are anthropogenic emissions from HTAP inventory in 2008 and 2010, respectively. The black and green solid lines show the total bottom-up emissions. The red and blue lines are posterior emissions from the hybrid inversion in 2008 and 2010.

From our top-down estimate, total NO_x emissions in Beijing decreased by 29.5% in July, 10.0% in August, 28.7% in September, and 22.3% in October

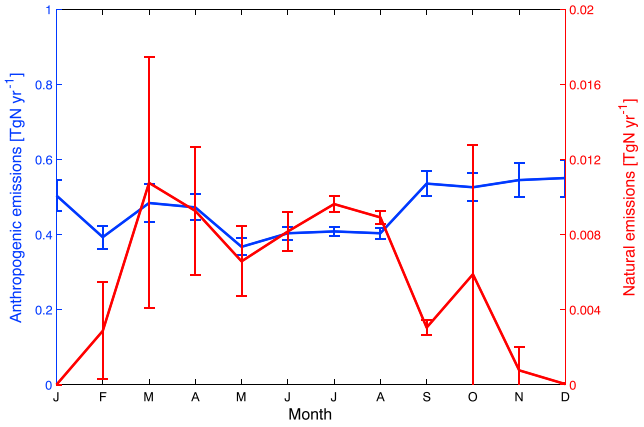

Figure 13. Posterior NO_x emissions (from hybrid inversion) summed from grid cells dominated by anthropogenic (blue line) and natural (red line) sources. Each month's emissions are the average value over the period of 2005–2012. Vertical bars show the standard deviation of monthly emissions over 8 years.

compared to average emissions for these months in other years. In July 2008, our optimized total monthly emission in Beijing has reduced by 30% (1.9×10^6 kg N mon^{-1}) compared to average July emissions in other studied years. The relative magnitude of this reduction is fairly consistent with reductions in bottom-up anthropogenic emissions of ~25% (8.3×10^5 kg N mon^{-1}), after the emission limits measures implemented in late July of 2008 [*Wang et al.*, 2010]. Discrepancies can be explained by the inclusion of natural emissions in our studies.

5.2. Comparisons With Other Top-down Studies, Bottom-Up Inventories and In Situ Measurement

Our optimized national NO_x emission in 2007 (7.2 Tg N yr^{-1}) is about 4% less than the top-down fossil fuel NO_x emission of 7.5 Tg N yr^{-1} based on an inversion in July 2007, by *Zhao and Wang* [2009]. Our posterior emission in 2008 (7.0 Tg N yr^{-1}) is 3% larger than the estimate of 6.8 Tg N yr^{-1} in *Lin et al.* [2010], which is based on an inversion in July 2008. Discrepancy between our posterior and estimates from these two studies can be caused by differences in inversion method, prior emissions, and studied period, i.e., our annual budget is calculated by averaging monthly emissions in each year, whereas estimates in these two studies are extrapolated based only on emissions in July. The contribution of Taiwan's annual emission to the national annual emission is between 1.4% to 2.5% during the studied period, and therefore, exclusion of Taiwan's emission in this study would not be a key contributor to the difference between our result and those in other studies.

We find a generally increasing trend of NO_x emissions in western China, which is consistent with *Cui et al.* [2016] in terms of contributions of anthropogenic emissions to observed NO_2 column trends, even though we are using different retrieval products which have different trends as shown in Figure 8 and described in section 4.2. The anthropogenic contributions they reported are less influenced by meteorology and are more directly comparable to our posterior emissions. We also find an increase of emissions from 2011 to 2012 in Xinjiang and Yunnan, supporting the implication in *Cui et al.* [2016] of an underestimate in the official emission inventory. The year-to-year variations (e.g., decrease of emissions in 2008 over China and Beijing) are more clear in our posterior than in *Cui et al.* [2016], since we present variations on annual time scales. When

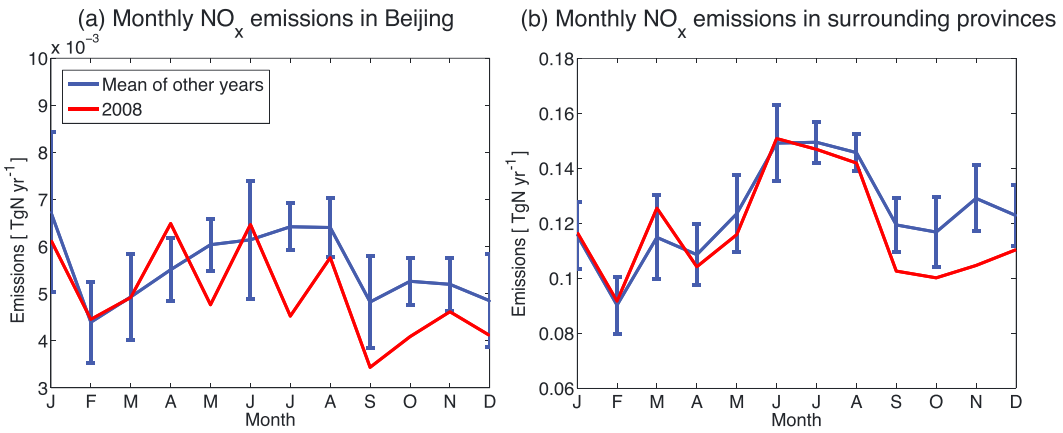

Figure 14. Monthly hybrid NO_x posterior emissions in Beijing and surrounding city and provinces (Tianjin, Hebei Province, Shandong Province, and Shanxi Province) in 2008 and average of other years. The vertical bars show the standard deviation of monthly emissions in other years.

compared to top-down emissions from *Mijling et al.* [2013] using GOME-2 observations and the Daily Emission estimates Constrained by Satellite Observations (DECSO) algorithm (cyan line in the first panel of Figure 9), our posterior NO_x emissions are 10% to 19% larger from 2007 to 2009, almost the same in 2010, and 8% smaller in 2011. The growth rates of our posterior over East China are also smaller than that from *Mijling et al.* [2013] over the same region. The 16% increase of posterior NO_x emissions from 2005 to 2012 is close to the 22–23% increase reported in *Miyazaki et al.* [2017] in the same period, although they are using a different model (MIROC-Chem), different satellite observations (assimilate multiple species from multiple sensors), and a different inversion approach (ensemble square root filter) than our study. The average posterior of 2008 and 2010 from *Miyazaki et al.* [2017] (6.19 Tg N yr^{-1}) is also lower than our posterior mean of these two years (7.27 Tg N yr^{-1}). Trends of our emissions and NO_2 columns in several cities, such as Beijing, Shanghai, and Tianjin, are not exactly the same as the trends in *Duncan et al.* [2016], even after performing the multivariate linear regression method described in *Lamsal et al.* [2015], because trends in different regions across the area we define for each city can be different, and our resolution of 0.5° × 0.667° covers larger areas than those in their study (0.1° × 0.1°).

Comparison of our total posterior emissions with total bottom-up emissions are shown in the first plot of Figure 9. We consider the anthropogenic bottom-up inventories from the MEIC [*Xia et al.*, 2016], and natural emissions from the bottom-up inventory described in section 2.1. Over China, a generally increasing trend of our posterior emission from 2005 to 2011 is fairly consistent with the trend in the bottom-up inventory, which increases from about 7.65 Tg N yr^{-1} in 2005 to 9.90 Tg N yr^{-1} in 2010 (29% increase) based on MEIC anthropogenic emissions, and increases from 6.96 Tg N yr^{-1} in 2005 to 10.31 Tg N yr^{-1} in 2011 (48% increase) based on *Xia et al.* [2016]. Our posterior shows a 2% decrease from 2007 to 2008 as a consequence of the Olympic Games and economic recession, although only a slower growth rate of emissions during this period are evident in the bottom-up inventories. Starting from 2011, both the hybrid posterior and emissions from *Xia et al.* [2016] start to decrease. The bottom-up estimates shown in Figure 9 have both larger emissions and emission growth rates than our estimates, but our posterior emissions in 2006 (6.81 Tg N yr^{-1}) are larger than the bottom-up estimate of 6.33 Tg N yr^{-1} from INTEX-B for the same year [*Zhang et al.*, 2009]. Our underestimates can be attributed to the weighting of satellite error in our hybrid inversions and the tendency of our posterior to underestimate the growth rate as described in section 3.4. The lower values from the top-down emissions from our study, *Mijling et al.* [2013] and *Miyazaki et al.* [2017] could also be influenced by factors such as model resolution errors in representing NO_2 columns at the satellite footprint scale [*Valin et al.*, 2011], systematic low biases in tropospheric OMI NO_2 retrievals from, e.g., use of spatially coarse prior profiles [*Laughner et al.*, 2016] and possibly high biased estimates of emissions and growth rate in the bottom-up inventory.

We also compare total optimized top-down NO_x emission in 2008 and 2010 with the sum of NO_x emissions from bottom-up inventories in corresponding years. In Figure 12, our posterior emissions have a general increasing trend from 2008 to 2010, whereas this trend is evident in the HTAP inventory but not in the total bottom-up (including natural sources) emissions. Top-down emissions are more consistent with bottom-up emissions during summertime but have lower values the rest of the year. This is similar to the difference in column density observed by satellite and simulated by GEOS-Chem, suggesting that prior emissions or meteorology are better in summertime. In wintertime, longer NO_x lifetime may also lead to larger uncertainties and differences between the model and OMI observations.

We also attempt to evaluate the trend of our total posterior NO_x emission in Beijing in August from 2006 to 2010 with ground-based measurements by *Zhang et al.* [2014], located at (39.99°N, 116.31°E), although the findings are limited. The surface measurement of NO_2 concentration in *Zhang et al.* [2014] show a 5% decrease from 2006 to 2007, a 41% decrease in 2008, a 48% increase in 2009 and a 5% decrease in 2010. Our posterior NO_2 surface concentration has a very different trend compared to this in situ measurement ($R = -0.54$ for prior, $R = 0.33$ for posterior), likely as our posterior concentration averaged over a grid cell are not directly comparable with surface measurements at one single site. However, our posterior emission have the same decrease in August 2008, as the ground-based measurement, which reflects the emission reduction during the Beijing Olympic Games inside and surrounding Beijing.

6. Conclusions and Discussions

In this study we combine two traditional inversion methods to facilitate more accurate decadal-scale NO_x emission inversions in China. When the initial guess and true emissions follow the same spatial structure,

performance of a newly derived mass balance approach has smaller NMSE (<25%) than a 4D-Var inversion with off-diagonal error covariance matrix. NMSE of the 4D-Var posterior is even smaller than that of the mass balance posterior when the initial guess is spatially different from the true emissions (67% smaller when the initial guess is low, and 96% smaller when the initial guess is high). We then develop a hybrid inversion with 4D-Var method applied first to improve emissions in a base year, followed by further improvement in each individual year using the mass balance approach. This hybrid method only takes one eighth of the time needed by standard 4D-Var to finish an 8 year inversion and can better capture trends and spatial variability of NO_x emissions as demonstrated through pseudo inversions than mass balance ($R = 0.977$ using hybrid versus $R = 0.920$ using mass balance when initial guess is low, and $R = 0.968$ using hybrid versus $R = 0.965$ using mass balance when initial guess is high), and leads to better correlation with OMI column density over China ($R = 0.948$ using hybrid inversion versus $R = 0.911$ using mass balance).

Using this hybrid inversion approach, an overall increase of both NO_2 column densities (by 9%) and NO_x emissions (by 16%) in China is detected; however, we also find important regional variations in these trends, as well as regions in which trends in emissions and NO_2 columns are not synchronized. The former is evident in emission trends, in particular, grid cells that are unique from their surroundings, such as the increase of emissions in Beijing in contrast to the decrease of emissions in Mentougou district of Beijing. The latter, owing to the influence from meteorology, has important implications for emissions trend studies. Meteorological factors are found to cause a maximum of 29.6% annual change in NO_2 columns and lead to a 7.7% increase of national NO_2 column density in 2012 (compared to 2011 level), even though NO_x emissions decreased between these years. Within our studied period, NO_x emissions generally rise in the Yangtze River Delta Economic Zone (8%), decrease in Guangdong Province (6%), and both increase and decrease in Beijing, depending on the year. Overall, emissions decrease by 10–26% in major cities (e.g., Mentougou district of Beijing, Guangzhou, Shenzhen, Zhuhai, Hong Kong, and Macau) from 2005 to 2012, whereas emissions increase in the rest of China. From 2010 to 2012, decreases of NO_x emissions occur in the broader area of Beijing, Tianjin, Hebei Province, Henan Province, Shandong Province, Hubei Province, and Pearl River Delta area, coinciding with China's enforcement of its twelfth "Five Year Plan," which specified for the first time a national commitment to reduce NO_x emissions. Decreases of NO_x emissions (by ~10.0–29.5%) are also found during the Beijing Olympic and Paralympic Games, suggesting effective pollution control strategies, during that period, and consistency between our results and previous studies [e.g., *Wang et al.*, 2010].

We evaluate the hybrid inversion and its ability to detect variation of NO_x emissions by comparing posterior emissions with bottom-up inventories and in situ NO_2 concentration measurements. Our posterior estimates of anthropogenic NO_x emissions are 7–20% smaller and have smaller growth rate when compared to the MEIC inventory. Monthly posterior emissions have the same seasonality in 2008 and 2010 with the HTAP inventory but have more interannual variations.

The inversion is based on the assumption that observations are unbiased. We do not estimate hybrid posterior uncertainty in this study because it depends on uncertainty of 4D-Var posterior emissions in 2010, which is difficult to estimate rigorously [*Bousserez et al.*, 2015]. NASA standard and DOMINO products for OMI NO_2 retrievals can be different by 50% over densely populated area in the studied domain. Based on this discrepancy in retrieval products and differences caused by data processing approaches, we recognized that our posterior emissions are more robust in Yangtze River Delta, Xinjiang, Ningxia, and Inner Mongolia. Several factors leading to uncertainties in our top-down emission inventory are as follows:

1. Uncertainties in CO, SO_2 and other species' emissions on NO_2 columns are not considered when performing the inversion. Also, all changes of NO_x emissions are penalized according to uncertainties in anthropogenic emissions. However, neither of these factors likely lead to large uncertainties since sensitivities of NO_2 columns to other species and sectors are more than 2 orders of magnitude smaller than sensitivities to anthropogenic NO_x emissions, except in summertime (when sensitivity with respect to lightning NO_x has the largest value) when the prior model performs well, regardless.
2. The simple mass balance approach is found to have considerable error, owing to transport and chemistry. However, other more sophisticated mass balance methods that change emissions iteratively [e.g., *Ghude et al.*, 2013] account for the nonlinear response of NO_2 column by a perturbation approach [e.g., *Lamsal et al.*, 2011] and use a kernel to account for the influence of transport [e.g., *Toenges Schuller et al.*, 2006; *Boersma et al.*, 2008] may perform better.

3. We use an error covariance matrix with a constant error correlation length scale across all grid cells. Future refined estimates should consider variable length scales that more realistically reflect correlation of NO_x emissions from different sectors in different regions.
4. The amount of satellite observations available each year are different after data filtering, as there are more observations affected by row anomalies after 2009, which implies that posterior emissions in the first few years may be more reliable.
5. The tropospheric OMI NO_2 retrievals we employed in this study are likely to have low biases owing to the use of spatially coarse prior profiles [*Laughner et al.*, 2016].
6. The relative coarse model resolution used in this study could lead to uncertainties in NO_2 loss rate and therefore biases in predicted NO_2 columns [*Valin et al.*, 2011].

Appendix A: Derivation of Mass Balance Equations

Here we derive mass balance equations according to maximum likelihood estimation given prior emission $E_a(i,j)$ and top-down estimate $E_t(i,j)$ (defined in equation (A1)), which are assumed to have lognormally distributed errors. These are different from the original equations from *Martin et al.* [2003a], wherein the mean and standard deviation of this lognormal distribution were assumed (incorrectly) be $\ln(E)$ and $\ln(\mu)$, respectively. In the simplest case, a top-down NO_x emission at (i,j) is

$$E_t(i,j) = E_a(i,j)\frac{\mathrm{SCD}_{\mathrm{obs}}(i,j)}{\mathrm{SCD}_{\mathrm{GC}}(i,j)}. \tag{A1}$$

We derive our mass balance equation for emissions scaling factors based on maximum likelihood estimation, which weights top-down and bottom-up emissions by their uncertainties. We define a random variable X, where

$$X = \begin{cases} 1 & \text{if } E(i,j) \text{ is the true emission} \\ 0 & \text{if } E(i,j) \text{ is not the true emission} \end{cases} \tag{A2}$$

Assuming log-normal distribution for emissions, the probability that a given value $E(i,j)$ is the true emission can therefore be expressed as follows:

$$\begin{aligned} P(X=1) = {} & \frac{1}{\sqrt{2\pi}E(i,j)\sigma_a(i,j)} \exp\left[-\frac{(\ln E(i,j)-\mu_a(i,j))^2}{2\sigma_a^2(i,j)}\right] \\ & \times \frac{1}{\sqrt{2\pi}E(i,j)\sigma_t(i,j)} \exp\left[-\frac{(\ln E(i,j)-\mu_t(i,j))^2}{2\sigma_t^2(i,j)}\right] \end{aligned} \tag{A3}$$

$$\mu_a(i,j) = \ln \frac{E_a(i,j)}{\sqrt{1+\epsilon_a^2(i,j)}} \tag{A4}$$

$$\mu_t(i,j) = \ln \frac{E_t(i,j)}{\sqrt{1+\epsilon_t^2(i,j)}} \tag{A5}$$

$$\sigma_a^2(i,j) = \ln\left(1+\epsilon_a^2(i,j)\right) \tag{A6}$$

$$\sigma_t^2(i,j) = \ln\left(1+\epsilon_t^2(i,j)\right) \tag{A7}$$

where ϵ_t and ϵ_a are relative errors, μ_t and μ_a are location parameters, and σ_t and σ_a are scale parameters of the top-down and prior emissions, respectively. Since error in top-down emissions mainly come from satellite observations, we use an average uncertainty of these observations (~20%) for ϵ_t. ϵ_a is set as 40% following assumptions in section 3.1.1. To account for instrument detection limits, the mass balance inversion is only applied to grid cells in which the observed column density is greater than 1.5×10^{15} molecules cm^{-2}. This value is higher than the detection limit in 4D-Var assimilation, because we are calculating limit for monthly averaged NO_2 column density here, whereas in 4D-Var the limit corresponds to individual observations.

An emission from maximum likelihood estimation (MLE) has the greatest probability to be the true state given prior and top-down emission, and would satisfy

$$\frac{\mathrm{d}\ln P(X=1)}{\mathrm{d}E}=0. \tag{A8}$$

Solving this equation, we get

$$E(i,j)=\exp\left[\frac{\ln\left(1+\epsilon_t^2(i,j)\right)\times\ln\frac{E_a(i,j)}{\sqrt{1+\epsilon_a^2(i,j)}}+\ln\left(1+\epsilon_a^2(i,j)\right)\times\ln\frac{E_t(i,j)}{\sqrt{1+\epsilon_t^2(i,j)}}}{\ln\left(1+\epsilon_t^2(i,j)\right)+\ln\left(1+\epsilon_a^2(i,j)\right)}\right.$$
$$\left.-\frac{2\ln\left(1+\epsilon_a^2(i,j)\right)\ln\left(1+\epsilon_t^2(i,j)\right)}{\ln\left(1+\epsilon_t^2(i,j)\right)+\ln\left(1+\epsilon_a^2(i,j)\right)}\right]. \tag{A9}$$

This optimized emission balances bottom-up and top-down emissions by weighting these two estimates in terms of their relative errors. The emission scaling factor of this approach can then be expressed as

$$\sigma_{mb}(i,j)=\frac{E(i,j)}{E_a(i,j)}. \tag{A10}$$

If considering the local column at (i,j) is influenced by both its own emissions and transport of emissions from surrounding cells, we can apply an averaging kernel K following *Toenges Schuller et al.* [2006] and *Boersma et al.* [2008]. Here

$$\mathbf{K}=\frac{1}{k+8}\begin{bmatrix}1&1&1\\1&k&1\\1&1&1\end{bmatrix} \tag{A11}$$

The smoothing parameter k is set to be 8 since it maximizes the correlation between smoothed emissions and simulated column density in East Asia. The weight of changes in emissions considering transport from adjacent cell is

$$w=\frac{E^a_{i,j}}{\Sigma^1_{m=-1}\Sigma^1_{l=-1}K_{l,m}E^b_{i+l,j+m}} \tag{A12}$$

In the tests of this study, we only apply this weight w to the difference of $\frac{\mathrm{SCD_{obs}}}{\mathrm{SCD_{GC}}}$ from unity. Define $r=\frac{\mathrm{SCD_{obs}}}{\mathrm{SCD_{GC}}}$, the top-down emission is therefore

$$E_t=\begin{cases}((r-1)\times w+1)\times E_a & (r>1)\\ E_a & (r=1)\\ (1-(1-r)\times w)\times E_a & (r<1)\end{cases} \tag{A13}$$

We recognized that the sum of the modes of the lognormal distributions in each grid cell is not strictly the mode of the distribution of the aggregate emissions, but for this step we approximate the grid cell distributions as being normally distributed.

Acknowledgments
Z.Qu, D.K.Henze, Y.Wang, X.Xu, and J.Wang gratefully acknowledge support from National Aeronautics and Space Administration grant NNX13AK86G and Nicolas Bousserez for valuable discussion. This work utilized the Janus supercomputer, which is supported by the National Science Foundation (award CNS-0821794) and the University of Colorado Boulder. The Janus supercomputer is a joint effort of the University of Colorado Boulder, the University of Colorado Denver, and the National Center for Atmospheric Research. Janus is operated by the University of Colorado Boulder. The data used in this paper can be obtained from the corresponding author through e-mail (zhen.qu@colorado.edu).

References

Beirle, S., K. F. Boersma, U. Platt, M. G. Lawrence, and T. Wagner (2011), Megacity emissions and lifetimes of nitrogen oxides probed from space, *Science*, *333*(6050), 1737–1739, doi:10.1126/science.1207824.

Bey, I., D. J. Jacob, R. M. Yantosca, J. A. Logan, B. D. Field, A. M. Fiore, Q. Li, H. Y. Liu, L. J. Mickley, and M. G. Schultz (2001), Global modeling of tropospheric chemistry with assimilated meteorology: Model description and evaluation, *J. Geophys. Res.*, *106*(D19), 23,073–23,095, doi:10.1029/2001JD000807.

Bhatnagar, A. (2006), Environmental cardiology studying mechanistic links between pollution and heart disease, *Circ. Res.*, *99*(7), 692–705, doi:10.1161/01.RES.0000243586.99701.cf.

Boersma, K. F., D. J. Jacob, E. J. Bucsela, A. E. Perring, R. Dirksen, R. J. van der A, R. M. Yantosca, R. J. Park, M. O. Wenig, and T. H. Bertram (2008), Validation of OMI tropospheric NO_2 observations during INTEX-B and application to constrain NO_x emissions over the eastern United States and Mexico, *Atmos. Environ.*, *42*(19), 4480–4497, doi:10.1016/j.atmosenv.2008.02.004.

Bousserez, N., D. K. Henze, A. Perkins, K. W. Bowman, M. Lee, J. Liu, F. Deng, and D. B. A. Jones (2015), Improved analysis-error covariance matrix for high-dimensional variational inversions: Application to source estimation using a 3D atmospheric transport model, *Q. J. R. Meteorol. Soc.*, *141*(690), 1906–1921, doi:10.1002/qj.2495.

Bucsela, E. J., E. A. Celarier, M. O. Wenig, J. F. Gleason, J. P. Veefkind, K. F. Boersma, and E. J. Brinksma (2006), Algorithm for NO_2 vertical column retrieval from the ozone monitoring instrument, *IEEE Trans. Geosci. Remote Sens.*, *44*(5), 1245–1258, doi:10.1109/TGRS.2005.863715.

Bucsela, E. J., N. A. Krotkov, E. A. Celarier, L. N. Lamsal, W. H. Swartz, P. K. Bhartia, K. F. Boersma, J. P. Veefkind, J. F. Gleason, and K. E. Pickering (2013), A new stratospheric and tropospheric NO_2 retrieval algorithm for nadir-viewing satellite instruments: Applications to OMI, *Atmos. Meas. Tech.*, *6*(10), 2607–2626, doi:10.5194/amt-6-2607-2013.

Byrd, R. H., P. Lu, J. Nocedal, and C. Zhu (1995), A Limited memory algorithm for bound constrained optimization, *SIAM J. Sci. Comput.*, *16*(5), 1190–1208, doi:10.1137/0916069.

Castellanos, P., and K. F. Boersma (2012), Reductions in nitrogen oxides over Europe driven by environmental policy and economic recession, *Sci. Rep.*, *2*, 265, doi:10.1038/srep00265.

Castellanos, P., K. F. Boersma, and G. R. van der Werf (2014), Satellite observations indicate substantial spatiotemporal variability in biomass burning NO_x emission factors for South America, *Atmos. Chem. Phys.*, *14*(8), 3929–3943, doi:10.5194/acp-14-3929-2014.

Celarier, E. A., et al. (2008), Validation of Ozone Monitoring Instrument nitrogen dioxide columns, *J. Geophys. Res.*, *113*, D15S15, doi:10.1029/2007JD008908.

Chan, A. W. H., M. N. Chan, J. D. Surratt, P. S. Chhabra, C. L. Loza, J. D. Crounse, L. D. Yee, R. C. Flagan, P. O. Wennberg, and J. H. Seinfeld (2010), Role of aldehyde chemistry and NO_x concentrations in secondary organic aerosol formation, *Atmos. Chem. Phys.*, *10*(15), 7169–7188, doi:10.5194/acp-10-7169-2010.

Crutzen, P. J. (1979), The role of NO and NO_2 in the chemistry of the troposphere and stratosphere, *Annu. Rev. Earth Planet. Sci.*, *7*(1), 443–472, doi:10.1146/annurev.ea.07.050179.002303.

Cui, Y., J. Lin, C. Song, M. Liu, Y. Yan, Y. Xu, and B. Huang (2016), Rapid growth in nitrogen dioxide pollution over Western China, 2005–2013, *Atmos. Chem. Phys.*, *16*(10), 6207–6221, doi:10.5194/acp-16-6207-2016.

de Foy, B., J. L. Wilkins, Z. Lu, D. G. Streets, and B. N. Duncan (2014), Model evaluation of methods for estimating surface emissions and chemical lifetimes from satellite data, *Atmos. Environ.*, *98*, 66–77, doi:10.1016/j.atmosenv.2014.08.051.

Ding, J., R. J. van der A, B. Mijling, P. F. Levelt, and N. Hao (2015), NO_x emission estimates during the 2014 Youth Olympic Games in Nanjing, *Atmos. Chem. Phys.*, *15*(16), 9399–9412, doi:10.5194/acp-15-9399-2015.

Driscoll, C. T., G. B. Lawrence, A. J. Bulger, T. J. Butler, C. S. Cronan, C. EAGAR, K. F. Lambert, G. E. Likens, J. L. Stoddard, and K. C. Weathers (2001), Acidic deposition in the northeastern United States: Sources and inputs, ecosystem effects, and management strategies, *BioScience*, *51*(3), 180–198, doi:10.1641/0006-3568(2001)051[0180:ADITNU]2.0.CO;2.

Duncan, B. N., Y. Yoshida, B. de Foy, L. N. Lamsal, D. G. Streets, Z. Lu, K. E. Pickering, and N. A. Krotkov (2013), The observed response of Ozone Monitoring Instrument (OMI) NO_2 columns to NO_x emission controls on power plants in the United States: 2005–2011, *Atmos. Environ.*, *81*, 102–111, doi:10.1016/j.atmosenv.2013.08.068.

Duncan, B. N., L. N. Lamsal, A. M. Thompson, Y. Yoshida, Z. Lu, D. G. Streets, M. M. Hurwitz, and K. E. Pickering (2016), A space-based, high-resolution view of notable changes in urban NO_x pollution around the world (2005–2014), *J. Geophys. Res.*, *121*, 976–996, doi:10.1002/2015JD024121.

Evans, M. J., and D. J. Jacob (2005), Impact of new laboratory studies of N_2O_5 hydrolysis on global model budgets of tropospheric nitrogen oxides, ozone, and OH, *Geophys. Res. Lett.*, *32*, L09813, doi:10.1029/2005GL022469.

Ghio, A. J., C. Kim, and R. B. Devlin (2000), Concentrated ambient air particles induce mild pulmonary inflammation in healthy human volunteers, *Am. J. Respir. Crit. Care Med.*, *162*(3), 981–988, doi:10.1164/ajrccm.162.3.9911115.

Ghude, S. D., G. G. Pfister, C. Jena, R. J. van der A, L. K. Emmons, and R. Kumar (2013), Satellite constraints of nitrogen oxide (NO_x) emissions from India based on OMI observations and WRF-Chem simulations, *Geophys. Res. Lett.*, *40*, 423–428, doi:10.1002/grl.50065.

Giglio, L., J. T. Randerson, and G. R. Werf (2013), Analysis of daily, monthly, and annual burned area using the fourth-generation global fire emissions database (GFED4), *J. Geophys. Res. Biogeosci.*, *118*, 317–328, doi:10.1002/jgrg.20042.

Gu, D., Y. Wang, C. Smeltzer, and K. F. Boersma (2014), Anthropogenic emissions of NO_x over China: Reconciling the difference of inverse modeling results using GOME-2 and OMI measurements, *J. Geophys. Res. Atmos.*, *119*, 7732–7740, doi:10.1002/2014JD021644.

Gu, D., Y. Wang, R. Yin, Y. Zhang, and C. Smeltzer (2016), Inverse modelling of NO_x emissions over eastern China: Uncertainties due to chemical non-linearity, *Atmos. Meas. Tech.*, *9*(10), 5193–5201, doi:10.5194/amt-9-5193-2016.

Haagen-Smit, A. J. (1952), Chemistry and physiology of Los Angeles Smog, *Ind. Eng. Chem.*, *44*(6), 1342–1346, doi:10.1021/ie50510a045.

Hansen, P. C., (1999), The L-curve and its use in the numerical treatment of inverse problems, IMM Tech. Rep. 15/1999, Kongens Lyngby, Denmark.

Henze, D. K., A. Hakami, and J. H. Seinfeld (2007), Development of the adjoint of GEOS-Chem, *Atmos. Chem. Phys.*, *7*(9), 2413–2433, doi:10.5194/acp-7-2413-2007.

Henze, D. K., J. H. Seinfeld, and D. T. Shindell (2009), Inverse modeling and mapping US air quality influences of inorganic $PM_{2.5}$ precursor emissions using the adjoint of GEOS-Chem, *Atmos. Chem. Phys.*, *9*(16), 5877–5903.

Herron-Thorpe, F. L., B. K. Lamb, G. H. Mount, and J. K. Vaughan (2010), Evaluation of a regional air quality forecast model for tropospheric NO_2 columns using the OMI/Aura satellite tropospheric NO_2 product, *Atmos. Chem. Phys.*, *10*(18), 8839–8854.

Huang, X., Y. Song, M. Li, J. Li, Q. Huo, X. Cai, T. Zhu, M. Hu, and H. Zhang (2012), A high-resolution ammonia emission inventory in China, *Global Biogeochem. Cycles*, *26*, GB1030, doi:10.1029/2011GB004161.

Ialongo, I., J. Herman, N. Krotkov, L. Lamsal, K. F. Boersma, J. Hovila, and J. Tamminen (2016), Comparison of OMI NO_2 observations and their seasonal and weekly cycles with ground-based measurements in Helsinki, *Atmos. Meas. Tech.*, *9*(10), 5203–5212.

Jiang, Z., D. B. A. Jones, H. M. Worden, and D. K. Henze (2015), Sensitivity of top-down CO source estimates to the modeled vertical structure in atmospheric CO, *Atmos. Chem. Phys.*, *15*(3), 1521–1537, doi:10.5194/acp-15-1521-2015.

Janssens-Maenhout, G., et al. (2015), HTAP_v2.2: A mosaic of regional and global emission grid maps for 2008 and 2010 to study hemispheric transport of air pollution, *Atmos. Chem. Phys.*, *15*(19), 11,411–11,432, doi:10.5194/acp-15-11411-2015.

Jin, X., and T. Holloway (2015), Spatial and temporal variability of ozone sensitivity over China observed from the Ozone Monitoring Instrument, *J. Geophys. Res. Atmos.*, *120*, 7229–7246, doi:10.1002/2015JD023250.

Keller, C. A., M. S. Long, R. M. Yantosca, A. M. Da Silva, S. Pawson, and D. J. Jacob (2014), HEMCO v1.0: A versatile, ESMF-compliant component for calculating emissions in atmospheric models, *Geosci. Model Dev.*, *7*(4), 1409–1417, doi:10.5194/gmd-7-1409-2014.

Kim, S. W., A. Heckel, S. A. McKeen, G. J. Frost, E. Y. Hsie, M. K. Trainer, A. Richter, J. P. Burrows, S. E. Peckham, and G. A. Grell (2006), Satellite-observed U.S. power plant NO_x emission reductions and their impact on air quality, *Geophys. Res. Lett.*, *33*, L22812, doi:10.1029/2006GL027749.

Konovalov, I. B., M. Beekmann, A. Richter, and J. P. Burrows (2006), Inverse modelling of the spatial distribution of NO_x emissions on a continental scale using satellite data, *Atmos. Chem. Phys.*, *6*(7), 1747–1770, doi:10.5194/acp-6-1747-2006.

Kopacz, M., D. J. Jacob, D. K. Henze, C. L. Heald, D. G. Streets, and Q. Zhang (2009), Comparison of adjoint and analytical Bayesian inversion methods for constraining Asian sources of carbon monoxide using satellite (MOPITT) measurements of CO columns, *J. Geophys. Res.*, *114*, D04305, doi:10.1029/2007JD009264.

Krotkov, N. A., et al. (2016), Aura OMI observations of regional SO_2 and NO_2 pollution changes from 2005 to 2015, *Atmos. Chem. Phys.*, *16*(7), 4605–4629, doi:10.5194/acp-16-4605-2016.

Kurokawa, J., T. Ohara, T. Morikawa, S. Hanayama, G. Janssens-Maenhout, T. Fukui, K. Kawashima, and H. Akimoto (2013), Emissions of air pollutants and greenhouse gases over Asian regions during 2000–2008: Regional Emission inventory in ASia (REAS) version 2, *Atmos. Chem. Phys.*, *13*(21), 11,019–11,058, doi:10.5194/acp-13-11019-2013.

Lamsal, L. N., R. V. Martin, A. Padmanabhan, A. van Donkelaar, Q. Zhang, C. E. Sioris, K. Chance, T. P. Kurosu, and M. J. Newchurch (2011), Application of satellite observations for timely updates to global anthropogenic NO_x emission inventories, *Geophys. Res. Lett.*, *38*, L05810, doi:10.1029/2010GL046476.

Lamsal, L. N., B. N. Duncan, Y. Yoshida, N. A. Krotkov, K. E. Pickering, D. G. Streets, and Z. Lu (2015), U.S. NO_2 trends (2005–2013): EPA Air Quality System (AQS) data versus improved observations from the Ozone Monitoring Instrument (OMI), *Atmos. Environ.*, *110*, 130–143, doi:10.1016/j.atmosenv.2015.03.055.

Laughner, J. L., A. Zare, and R. C. Cohen (2016), Effects of daily meteorology on the interpretation of space-based remote sensing of NO_2, *Atmos. Chem. Phys.*, *16*(23), 15,247–15,264, doi:10.5194/acp-16-15247-2016.

Lee, D.-G., et al. (2011), Korean national emissions inventory system and 2007 air pollutant emissions, *Asian J. Atmos. Environ.*, *5*(4), 278–291, doi:10.5572/ajae.2011.5.4.278.

Li, M., et al. (2015), MIX: A mosaic Asian anthropogenic emission inventory for the MICS-Asia and the HTAP projects, *Atmos. Chem. Phys.*, *15*(23), 34,813–34,869, doi:10.5194/acpd-15-34813-2015.

Likens, G. E., F. H. Bormann, and N. M. Johnson (1972), Acid rain, *Environ. Sci. Policy Sustainable Dev.*, *14*(2), 33–40, doi:10.1080/00139157.1972.9933001.

Lin, J. T., M. B. McElroy, and K. F. Boersma (2010), Constraint of anthropogenic NO_x emissions in China from different sectors: A new methodology using multiple satellite retrievals, *Atmos. Chem. Phys.*, *10*(1), 63–78, doi:10.5194/acp-10-63-2010.

Lin, J. T., and M. B. McElroy (2011), Detection from space of a reduction in anthropogenic emissions of nitrogen oxides during the Chinese economic downturn, *Atmos. Chem. Phys.*, *11*(15), 8171–8188, doi:10.5194/acp-11-8171-2011.

Liu, H., D. J. Jacob, I. Bey, and R. M. Yantosca (2001), Constraints from ^{210}Pb and ^{7}Be on wet deposition and transport in a global three-dimensional chemical tracer model driven by assimilated meteorological fields, *J. Geophys. Res.*, *106*(D11), 12,109–12,128, doi:10.1029/2000JD900839.

Liu, F., Q. Zhang, R. J. van der A, B. Zheng, D. Tong, L. Yan, Y. Zheng, and K. He (2016), Recent reduction in NO_x emissions over China: Synthesis of satellite observations and emission inventories, *Environ. Res. Lett.*, *11*(11), 114002, doi:10.1088/1748-9326/11/11/114002.

Lu, Z., Q. Zhang, and D. G. Streets (2011), Sulfur dioxide and primary carbonaceous aerosol emissions in China and India, 1996–2010, *Atmos. Chem. Phys.*, *11*(18), 9839–9864, doi:10.5194/acp-11-9839-2011.

Lu, Z., D. G. Streets, B. de Foy, L. N. Lamsal, B. N. Duncan, and J. Xing (2015), Emissions of nitrogen oxides from US urban areas: Estimation from Ozone Monitoring Instrument retrievals for 2005–2014, *Atmos. Chem. Phys.*, *15*(18), 10,367–10.383, doi:10.5194/acp-15-10367-2015.

Martin, R. V., D. J. Jacob, K. Chance, T. P. Kurosu, P. I. Palmer, and M. J. Evans (2003a), Global inventory of nitrogen oxide emissions constrained by space-based observations of NO_2 columns, *J. Geophys. Res.*, *108*(D17), 4537, doi:10.1029/2003JD003453.

Martin, R. V., D. J. Jacob, R. M. Yantosca, M. Chin, and P. Ginoux (2003b), Global and regional decreases in tropospheric oxidants from photochemical effects of aerosols, *J. Geophys. Res.*, *108*(D3), 4097, doi:10.1029/2002JD002622.

McKeen, S. A., E. Y. Hsie, and S. C. Liu (1991), A study of the dependence of rural ozone on ozone precursors in the eastern United States, *J. Geophys. Res.*, *96*(D8), 15,377–15,394, doi:10.1029/91JD01282.

Mijling, B., and R. J. van der A (2012), Using daily satellite observations to estimate emissions of short-lived air pollutants on a mesoscopic scale, *J. Geophys. Res.*, *117*, D17302, doi:10.1029/2012JD017817.

Mijling, B., R. J. van der A, and Q. Zhang (2013), Regional nitrogen oxides emission trends in East Asia observed from space, *Atmos. Chem. Phys.*, *13*(23), 12,003–12,012, doi:10.5194/acp-13-12003-2013.

Miyazaki, K., H. J. Eskes, and K. Sudo (2012), Global NO_x emission estimates derived from an assimilation of OMI tropospheric NO_2 columns, *Atmos. Chem. Phys.*, *12*(5), 2263–2288, doi:10.5194/acp-12-2263-2012.

Miyazaki, K., H. Eskes, K. Sudo, K. F. Boersma, K. Bowman, and Y. Kanaya (2017), Decadal changes in global surface NO_x emissions from multi-constituent satellite data assimilation, *Atmos. Chem. Phys.*, *17*, 807–837, doi:10.5194/acp-17-807-2017.

Müller, J. F., and T. Stavrakou (2005), Inversion of CO and NO_x emissions using the adjoint of the IMAGES model, *Atmos. Chem. Phys.*, *5*(5), 1157–1186, doi:10.5194/acp-5-1157-2005.

Murray, L. T., D. J. Jacob, J. A. Logan, R. C. Hudman, and W. J. Koshak (2012), Optimized regional and interannual variability of lightning in a global chemical transport model constrained by LIS/OTD satellite data, *J. Geophys. Res.*, *117*, D20307, doi:10.1029/2012JD017934.

Nel, A. (2005), Air pollution-related illness: Effects of particles, *Science*, *308*(5723), 804–806, doi:10.1126/science.1108752.

Ohara, T., H. Akimoto, J. Kurokawa, N. Horii, K. Yamaji, X. Yan, and T. Hayasaka (2007), An Asian emission inventory of anthropogenic emission sources for the period 1980–2020, *Atmos. Chem. Phys.*, *7*(16), 4419–4444, doi:10.5194/acp-7-4419-2007.

Park, R. J., D. J. Jacob, B. D. Field, R. M. Yantosca, and M. Chin (2004), Natural and transboundary pollution influences on sulfate-nitrate-ammonium aerosols in the United States: Implications for policy, *J. Geophys. Res.*, *109*, D15204, doi:10.1029/2003JD004473.

Pickering, K. E., Y. Wang, W. K. Tao, C. Price, and J. F. Müller (1998), Vertical distributions of lightning NO_x for use in regional and global chemical transport models, *J. Geophys. Res.*, *103*(D23), 31,203–31,216, doi:10.1029/98JD02651.

Platt, U., and J. Stutz (2008), *Differential Optical Absorption Spectroscopy, Phys. of Earth and Space Environ.*, Springer, Berlin, doi:10.1007/978-3-540-75776-4.

Price, C., and D. Rind (1992), A simple lightning parameterization for calculating global lightning distributions, *J. Geophys. Res.*, *97*(D9), 9919–9933, doi:10.1029/92JD00719.

Russell, A. R., L. C. Valin, and R. C. Cohen (2012), Trends in OMI NO_2 observations over the United States: effects of emission control technology and the economic recession, *Atmos. Chem. Phys.*, *12*(24), 12,197–12,209, doi:10.5194/acp-12-12197-2012.

Ryerson, T. B., et al. (2001), Observations of ozone formation in power plant plumes and implications for ozone control strategies, *Science*, *292*(5517), 719–723, doi:10.1126/science.1058113.

Sauvage, B., R. V. Martin, A. van Donkelaar, X. Liu, K. Chance, L. Jaeglé, P. I. Palmer, S. Wu, and T. M. Fu (2007), Remote sensed and in situ constraints on processes affecting tropical tropospheric ozone, *Atmos. Chem. Phys.*, *7*(3), 815–838, doi:10.5194/acp-7-815-2007.

Singh, K., M. Jardak, A. Sandu, K. Bowman, M. Lee, and D. Jones (2011), Construction of non-diagonal background error covariance matrices for global chemical data assimilation, *Geosci. Model Dev.*, *4*(2), 299–316, doi:10.5194/gmd-4-299-2011.

Stavrakou, T., J. F. Müller, K. F. Boersma, I. De Smedt, and R. J. van der A (2008), Assessing the distribution and growth rates of NO_x emission sources by inverting a 10-year record of NO_2 satellite columns, *Geophys. Res. Lett.*, *35*, L10801, doi:10.1029/2008GL033521.

Stavrakou, T., J. F. Müller, K. F. Boersma, R. J. van der A, J. Kurokawa, T. Ohara, and Q. Zhang (2013), Key chemical NO_x sink uncertainties and how they influence top-down emissions of nitrogen oxides, *Atmos. Chem. Phys.*, *13*(17), 9057–9082, doi:10.5194/acp-13-9057-2013.

Streets, D. G., et al. (2003), An inventory of gaseous and primary aerosol emissions in Asia in the year 2000, *J. Geophys. Res.*, *108*(D21), 8809, doi:10.1029/2002JD003093.

Toenges Schuller, N., O. Stein, F. Rohrer, A. Wahner, A. Richter, J. P. Burrows, S. Beirle, T. Wagner, U. Platt, and C. D. Elvidge (2006), Global distribution pattern of anthropogenic nitrogen oxide emissions: Correlation analysis of satellite measurements and model calculations, *J. Geophys. Res.*, *111*, D05312, doi:10.1029/2005JD006068.

Turner, A. J., D. K. Henze, R. V. Martin, and A. Hakami (2012), The spatial extent of source influences on modeled column concentrations of short-lived species, *Geophys. Res. Lett.*, *39*, L12806, doi:10.1029/2012GL051832.

Valin, L. C., A. R. Russell, R. C. Hudman, and R. C. Cohen (2011), Effects of model resolution on the interpretation of satellite NO_2 observations, *Atmos. Chem. Phys.*, *11*(22), 11,647–11,655, doi:10.5194/acp-11-11647-2011.

Valin, L. C., A. R. Russell, and R. C. Cohen (2014), Chemical feedback effects on the spatial patterns of the NO_x weekend effect: A sensitivity analysis, *Atmos. Chem. Phys.*, *14*(1), 1–9, doi:10.5194/acp-14-1-2014.

van der Werf, G. R., J. T. Randerson, L. Giglio, G. J. Collatz, M. Mu, P. S. Kasibhatla, D. C. Morton, R. S. DeFries, Y. Jin, and T. T. v. Leeuwen (2010), Global fire emissions and the contribution of deforestation, savanna, forest, agricultural, and peat fires (1997–2009), *Atmos. Chem. Phys.*, *10*(23), 11,707–11,735, doi:10.5194/acp-10-11707-2010.

Vinken, G. C. M., K. F. Boersma, J. D. Maasakkers, M. Adon, and R. V. Martin (2014a), Worldwide biogenic soil NO_x emissions inferred from OMI NO_2 observations, *Atmos. Chem. Phys.*, *14*(18), 10,363–10,381, doi:10.5194/acp-14-10363-2014.

Vinken, G. C. M., K. F. Boersma, A. van Donkelaar, and L. Zhang (2014b), Constraints on ship NO_x emissions in Europe using GEOS-Chem and OMI satellite NO_2 observations, *Atmos. Chem. Phys.*, *14*(3), 1353–1369, doi:10.5194/acp-14-1353-2014.

Wang, S., M. Zhao, J. Xing, Y. Wu, Y. Zhou, Y. Lei, K. He, L. Fu, and J. Hao (2010), Quantifying the air pollutants emission reduction during the 2008 Olympic Games in Beijing, *Environ. Sci. Technol.*, *44*(7), 2490–2496, doi:10.1021/es9028167.

Wang, Y., D. J. Jacob, and J. A. Logan (1998), Global simulation of tropospheric O_3-NO_x-hydrocarbon chemistry: 3. Origin of tropospheric ozone and effects of nonmethane hydrocarbons, *J. Geophys. Res.*, *103*(D9), 10,757–10,767, doi:10.1029/98JD00156.

Wang, Y., M. B. McElroy, R. V. Martin, D. G. Streets, Q. Zhang, and T. M. Fu (2007), Seasonal variability of NO_x emissions over east China constrained by satellite observations: Implications for combustion and microbial sources, *J. Geophys. Res.*, *112*, D06301, doi:10.1029/2006JD007538.

Wells, K. C., et al. (2015), Simulation of atmospheric N_2O with GEOS-Chem and its adjoint: Evaluation of observational constraints, *Geosci. Model Dev.*, *8*(10), 3179–3198, doi:10.5194/gmd-8-3179-2015.

Xia, Y., Y. Zhao, and C. P. Nielsen (2016), Benefits of China's efforts in gaseous pollutant control indicated by the bottom-up emissions and satellite observations 2000–2014, *Atmos. Environ.*, *136*, 43–53, doi:10.1016/j.atmosenv.2016.04.013.

Xu, X., J. Wang, D. K. Henze, W. Qu, and M. Kopacz (2013), Constraints on aerosol sources using GEOS-Chem adjoint and MODIS radiances, and evaluation with multisensor (OMI, MISR) data, *J. Geophys. Res. Atmos.*, *118*, 6396–6413, doi:10.1002/jgrd.50515.

Yienger, J. J., and H. Levy (1995), Empirical model of global soil-biogenic NO_x emissions, *J. Geophys. Res.*, *100*(D6), 11,447–11,464, doi:10.1029/95JD00370.

Zhang, Q., et al. (2007), NO_x emission trends for China, 1995–2004: The view from the ground and the view from space, *J. Geophys. Res.*, *112*, D22306, doi:10.1029/2007JD008684.

Zhang, Q., et al. (2009), Asian emissions in 2006 for the NASA INTEX-B mission, *Atmos. Chem. Phys.*, *9*(14), 5131–5153, doi:10.5194/acp-9-5131-2009.

Zhang, Q., B. Yuan, M. Shao, X. Wang, S. Lu, K. Lu, M. Wang, L. Chen, C. C. Chang, and S. C. Liu (2014), Variations of ground-level O_3 and its precursors in Beijing in summertime between 2005 and 2011, *Atmos. Chem. Phys.*, *14*(12), 6089–6101, doi:10.5194/acp-14-6089-2014.

Zhao, B., S. X. Wang, H. Liu, J. Y. Xu, K. Fu, Z. Klimont, J. M. Hao, K. B. He, J. Cofala, and M. Amann (2013), NO_x emissions in China: Historical trends and future perspectives, *Atmos. Chem. Phys.*, *13*(19), 9869–9897, doi:10.5194/acp-13-9869-2013.

Zhao, C., and Y. Wang (2009), Assimilated inversion of NO_x emissions over east Asia using OMI NO_2 column measurements, *Geophys. Res. Lett.*, *36*, L06805, doi:10.1029/2008GL037123.

Zheng, F., T. Yu, T. Cheng, X. Gu, and H. Guo (2014), Intercomparison of tropospheric nitrogen dioxide retrieved from ozone monitoring instrument over china, *Atmos. Pollut. Res.*, *5*(4), 686–695.

Zhu, C., R. H. Byrd, P. Lu, and J. Nocedal, (1994), L-BFGS-B: A limited memory FORTRAN code for solving bound constrained optimization problems, Tech. Rep. No. NAM-11, EECS Dept., Northwestern Univ., Evanston, Ill., [Available at users.iems.northwestern.edu.]